A geometry-preserving finite volume method for conservation laws on curved geometries

Abdelaziz Beljadid, Philippe G. LeFloch, Abdolmajid Mohammadian

A geometry-preserving finite volume method for conservation laws on curved geometries

Abdelaziz Beljadid[1], Philippe G. LeFloch[2], and Abdolmajid Mohammadian[3]

Abstract

We consider nonlinear hyperbolic equations posed on curved geometries and investigate a geometry-preserving, second-order accurate, finite volume method. For definiteness, we study the so-called class of "geometric Burgers equations" posed on the sphere and defined from a prescribed potential function. Despite its apparent simplicity, this model exhibits very complex wave phenomena that are not observed in absence of geometrical effects. Our method is based on second-order finite volume approximations and generalized Riemann solvers. Our main contribution is a rigorous investigation of the properties of discontinuous solutions. In particular, we demonstrate the contraction property, the time-variation monotonicity property, and the entropy monotonicity property (in all norms). We also study the late-time asymptotic behavior of solutions, which is found to depend on the properties of the flux vector and results from the nonlinear interactions between hyperbolic waves and the underlying geometry.

1 Introduction

This paper is devoted to nonlinear hyperbolic problems, which can be based on conservation laws or, more generally, balance laws and are posed on curved geometries, for instance a surface. Our objective is to design robust and efficient numerical approximation methods which allow to compute discontinuous solutions and preserve the fundamental structure of the partial differential equations, especially geometry-related properties. Hence, our goal is to design and numerically investigate geometry-preserving, high-order accurate, finite volume methods. We advocate the use of a (geometric) formulation of the finite volume method based on the intrinsic (or covariant) form of the equations, rather then the coordinate expression which is more commonly used.

[⋆⋆]Department of Civil Engineering, University of Ottawa, 161 Louis Pasteur, Ottawa, Ontario, K1N6N5, Canada, E-mail: abelj016@uottawa.ca.
[⋆] Laboratoire Jacques-Louis Lions & Centre National de la Recherche Scientifique, Université Pierre et Marie Curie (Paris 6), 75258 Paris, France.
Email: contact@philippelefloch.org.

In this manner, by properly taking into account the effects induced by the geometry, we can design methods that are, both, accurate and robust.

We do not a priori restrict ourself to a specific discretization technique, but, rather, we aim at comparing various strategies such as generalized Riemann solvers, second-order centered schemes, etc. Compressible fluid dynamics provide a large variety of problems which involve geometrical features. The prototype example is the system of shallow water on the sphere with topography, which describe fluid flows on the surface of the Earth for instance, in connections with weather predictions [8].

Motivated by numerous applications in fluid dynamics, the study of hyperbolic conservation laws posed on curved manifolds were recently initiated in the mathematical and numerical literature. We build here on the work by Ben-Artzi and LeFloch [5] who proposed to rely on an analogue of the inviscid Burgers equation for curved geometry and, more generally, various classes of hyperbolic conservation laws on manifolds. Since Burgers equations has played such an important role in the development of shock-capturing schemes for compressible fluid problems, it is also expected that the class of "geometric Burgers models" should provide an ideal simplified setup in order to design and test geometric-preserving shock-capturing scheme. The mathematical properties of entropy solutions to conservation laws on manifolds were then extensively investigated by LeFloch and co-authors [1,2,5,4] and [10]– [13].

Scalar conservation laws will thus be our starting point in the present work and, next, will extend our methodology and conclusions to other hyperbolic equations, such as the shallow water system. In the present paper, we thus focus on **geometric Burgers models** of the form

$$\partial_t u + \mathrm{div} F(\cdot, u) = 0, \qquad u = u(t) : S^2 \to \mathbb{R}, \tag{1.1}$$

with unknown u defined on a curved space which we take to be the two-dimensional sphere S^2. The flux $F(\cdot, u)$ is a prescribed vector field defined on S^2, which depends on the unknown variable u as a parameter. (See Section 2, below.) We adopt the methodology proposed in [4] which relies on second–order approximations based on generalized Riemann problems (GRP). The **geometric GRP method** therein is further developed and numerically investigated. We observe that certain global quantities are conserved by entropy solutions to scalar conservation laws posed on curved geometries. Our aim is therefore to exhibit these global invariants and investigate to which extend they are preserved by (or remain monotone decreasing for) the approximation solutions generated by the geometric GRP method of [4]. We are also interested in investigating the large-time asymptotics of solutions, which is not understood by analytical method and will be here studied numerically. As we show it in this paper, by distinguishing between several classes of flux vector fields and initial conditions, we can exhibit a variety of nonlinear wave

phenomena.

Our analysis below shows that the geometric GRP method is consistent with the **maximum principle**

$$\|u(t')\|_{L^\infty(S^2)} \leq \|u(t)\|_{L^\infty(S^2)}, \qquad t' \geq t, \tag{1.2}$$

the **entropy stability property**

$$\|u(t')\|_{L^p(S^2)} \leq \|u(t)\|_{L^p(S^2)}, \qquad t' \geq t, \tag{1.3}$$

for all exponents $p \in [1, +\infty)$, as well as with the **time-variation diminishing property**

$$\|\partial_t u\|_{\mathcal{M}(S^2)}(t') \leq \|\partial_t u\|_{\mathcal{M}(S^2)}(t), \qquad t' \geq t, \tag{1.4}$$

where $\mathcal{M}(S^2)$ denotes the space of bounded measures defined on S^2. On the other hand, the **contraction property** (for any two entropy solutions u, v)

$$\|v(t) - u(t)\|_{L^1(S^2)} \leq \|v(0) - u(0)\|_{L^1(S^2)} \tag{1.5}$$

is violated by the scheme and is satisfied only by its first-order version.

Our analysis will distinguish between **foliated flux fields** and "generic" (or fully coupled) flux fields. Geometric conservation laws with foliated flux are a combination of linear transport and nonlinear hyperbolic equations, in the sense that the solutions are simply transported within the level sets and (exact) solutions can be defined in each level set, independently of the level parameter. Under some assumption concerning the transport speed along the level sets (as shown in Test 1-a, below), the solutions can be globally preserved within the entire sphere S^2 in a suitably defined "moving frame". For foliated flux fields satisfying a suitable nonlinearity condition, the solutions converge to their constant average in each level set (as shown in Test 5, below). This latter case includes, in particular, solutions which converge to constant values in independent domains on the sphere (as illustrated in Tests 2 and 3, below).

For fully coupled flux fields, the solutions converge to constant values in independent domains on the sphere. The number of constants depends on the existence of the curves that split the sphere in independent parts, as we define below. In the case of the generic flux, the scalar function of the gradient can be decomposed in several homogeneous terms. The term is said to be homogeneous if it corresponds to a foliated flux field. The behavior of the solution is greatly influenced by the homogeneous terms of high order. The asymptotic convergence to constant values is influenced on the nature of the terms of the generic flux and the initial condition.

The outline of this paper is as follows. In Section 2, we describe the geometric conservation laws and the properties of their entropy solutions, and next

present examples of flux fields and classes of solutions of particular interest. Section 3 is devoted to the description and analysis of the geometric GRP method. Section 4 presents some numerical tests for linear foliated fluxes. In Sections 5 and 6, numerical tests are performed for nonlinear foliated fluxes. In Sections 7 and 8, we present a variety of numerical test cases for fully coupled flux vector fields as well as further tests to study the asymptotic convergence of solutions. Finally, Section 9 contains concluding remarks.

2 Geometric Burgers models on the sphere

2.1 Geometric hyperbolic conservation laws on manifolds

We are primarily interested in nonlinear hyperbolic equations posed on the sphere, but since the mathematical theory supporting the study in the present paper has been developed for general manifolds endowed with a volume form, as we now explain, so we introduce it at this level of generality first. Fix any compact n-manifold M endowed with a volume form ω with L^∞ regularity. Given a **flux vector field** $F = F(x,u) \in T_xM$ depending on the real parameter u, we consider the **geometric hyperbolic balance law**

$$\partial_t u + \mathrm{div}_\omega F(\cdot,u) = 0 \quad \text{ in } \mathbb{R}_+ \times M, \tag{2.1}$$

with unknown $u : \mathbb{R}_+ \times M \to \mathbb{R}$. We impose that the flux is **geometry-compatible,** in the sense that

$$\mathrm{div}_\omega F(\cdot,u) = 0, \qquad u \in \mathbb{R}, \tag{2.2}$$

which is equivalent to say that constants are (trivial) solutions of the conservation law. Then, weak solutions are understood in the following sense: for every test-function $\theta = \theta(t,x)$,

$$\iint_{\mathbb{R}_+\times M} \Big(\partial_t\theta(t,x)\, u(t,x) + \partial_j\theta(t,x) F^j(x,u(t,x))\Big)\, \omega(x) dt dx = 0, \tag{2.3}$$

where F^j denote the components of the vector field F in an arbitrary coordinate chart $x = (x^j)_{1\le j\le n}$. Here, we have identified the volume form ω with its expression ωdx in local coordinates (and, for simplicity in order to state (2.3), we have assumed that the manifold is covered by a single chart).

To any equation (2.1) with flux field satisfying the condition (2.2), we can associate a unique **semi–group of entropy solutions** characterized as follows: given any $u_0 \in L^\infty(M)$, there exists a unique entropy solution $u \in L^\infty(\mathbb{R}_+ \times M)$ to the initial value problem

$$\begin{aligned} &\partial_t U(u) + \mathrm{div}_\omega G(\cdot,u) \le 0, \qquad U'' \ge 0, \\ &u(0) = u_0, \end{aligned} \tag{2.4}$$

in which for every convex function $U : \mathbb{R} \to \mathbb{R}$ we have introduced the corresponding entropy flux $G = G(x, u) \in T_x M$ such that $\partial_u G := U' \, \partial_u F$. The inequalities in (2.4) are refered to as the **entropy inequalities.**

Moreover, this semi-group of entropy solutions satisfies several fundamental properties:

- **Entropy stability property:** for all $p \in [1, \infty)$ and $t \geq 0$

$$\|u(t)\|_{L^p_\omega(M)} \leq \|u(0)\|_{L^p_\omega(M)}, \tag{2.5}$$

  which also implies the **maximum principle** (by letting $p \to +\infty$):

$$\|u(t)\|_{L^\infty(M)} \leq \|u(0)\|_{L^\infty(M)}. \tag{2.6}$$

- **The L^1 contraction property**: given any two entropy solutions u, v and for all times $t \geq 0$

$$\|v(t) - u(t)\|_{L^1_\omega(M)} \leq \|v(0) - u(0)\|_{L^1_\omega(M)}. \tag{2.7}$$

- **The time-variation diminishing property:** given any entropy solution u

$$\|\partial_t u\|_{\mathcal{M}}(t) \leq \|\partial_t u\|_{\mathcal{M}}(0), \qquad t \geq 0. \tag{2.8}$$

We thus have a natural generalization of Kruzkov's theory [9] to a manifold [1,2,10,13]. Geometry-independent bounds hold, which are very useful in design and testing discrete approximation schemes.

The low regularity of the volume form allows us to also include *shock wave in the geometry* (which is relevant to model earthquakes in the context of the shallow water system, for instance).

2.2 The models of interest in this paper

In the applications, the manifold M is often defined via an embedding in the higher-dimensional Euclidian space $\mathbb{R}^N$. For simplicity, in the rest of this paper we concentrate on surfaces and, specifically, the two-sphere S^2 endowed with a volume form ω and embedded in $\mathbb{R}^3$. We denote by S^2 the unit sphere embedded in $\mathbb{R}^3$ and endowed with the canonical volume form induced by the Euclidian metric.

By denoting by $\nabla_{S^2_\omega}$ the covariant derivative operator on the sphere $S^2_\omega \subset \mathbb{R}^3$, we now express the conservation law in the form

$$\partial_t u + \nabla_{S^2_\omega} \cdot (F(\cdot, u)) = 0, \tag{2.9}$$

or equivalently, in local coordinates, we can pose the problem on the unit sphere with a weight function $\omega = \omega(x)$

$$\partial_t u(t,x) + \frac{1}{\omega(x)} \nabla_{S^2} \cdot \Big(\omega(x)\, F(x, u(t,x)) \Big) = 0. \tag{2.10}$$

Flux vector tangent to the sphere can always be expressed in the form

$$F(x,u) = n(x) \wedge \Phi(x,u), \qquad x \in S^2,\ u \in \mathbb{R}, \tag{2.11}$$

where $\Phi = \Phi(x,u)$ is a u-dependent vector field defined in the ambient space $\mathbb{R}^3$, and $n = n(x)$ denotes the unit normal vector to the sphere.

As explained earlier, we are primarily interested in geometry-compatible flux vectors satisfying, by definition,

$$\nabla \cdot (F(\cdot, \bar{u})) = 0, \qquad \bar{u} \in \mathbb{R}. \tag{2.12}$$

Especially, the broad class of **gradient-type flux vector fields** is defined by

$$\Phi(x,\bar{u}) = \nabla h(x,\bar{u}), \qquad x \in S^2, \quad \bar{u} \in \mathbb{R}, \tag{2.13}$$

in which $h = h(x,\bar{u})$ is an arbitrary scalar function and ∇ denotes the gradient operator in $\mathbb{R}^3$. Under these conditions, the flux vector field reads

$$F(x,\bar{u}) = n(x) \wedge \nabla h(x,\bar{u}), \qquad x \in S^2, \quad \bar{u} \in \mathbb{R} \tag{2.14}$$

and we then refer to (2.9) as the **geometric Burgers equations on the sphere** and are determined by a scalar function $h : \mathbb{R}^3 \times \mathbb{R} \to \mathbb{R}$.

We will refer to the function h as the **scalar potential** of the equation. For instance, if h is chosen to be a linear function in the space variable, then Φ is independent of x but its projection on the tangent space of the sphere is still "non-trivial".

2.3 Classes of flux vector fields

2.3.1 Foliated flux vector fields

A flux field $F(x,u)$ depends on both the state variable u and the space variable x. Roughly speaking, the dependency in x drives the propagation of the waves, while the dependency in u may induce the formation of shocks in the solutions. Some aspects of the influence of the parameters x and u on the evolution of the solution are observed and analyzed in various cases studied in the numerical tests.

Let us illustrate with two examples, which we will later investigate numerically. In Test 1-a discussed below, the directions of propagation depend on the space

variable x only, which is achieved by choosing the potential function $h(x,u) = -x_3 u$. The solutions are simply transported so that the directions of this transportation (or level sets) are defined by the curves $x_3 = c$, where $c \in [-1,1]$ is any real constant. Having here a potential which is linear in u, no shock wave can form during the evolution (from regular data, say).

On the other hand, when the potential function is chosen to be $h(x,u) = -x_3 \frac{u^2}{2}$ (as will be investigated in Test 5, below), again the directions of evolution are given by the curves $x_3 = c$, where $c \in [-1,1]$ is any real constant. For this case, shock waves do form in finite time from "general" initial data: this feature is due to the nonlinear dependency of h in the variable u. These shocks generate rather large variations in solutions along the level sets. We still have formation of shocks within each level set and the solution can be computed independently in each of these lines. We will observe later that each solution converges asymptotically to a *constant value* on each line.

To conduct a rigorous numerical analysis and with the examples above in mind, it is useful to introduce some new definitions, which allows us to have the classification of the flux vectors and the type of evolution of solutions. Consider first the dependency in the variable $x \in S^2$. Our analysis has found that the following parameterized level sets $\Gamma_{C,u} = \left\{ x \in \mathbb{R}^3 \,\middle/\, h(x,u) = C \right\}$ play a central role and that the following definition is most relevant.

Definition 2.1 *A gradient flux vector field $F(x,u) = n(x) \wedge \nabla_x h(x,u)$ defined on the sphere S^2 and associated with a potential function h is called a* **foliated flux field** *if the associated family of level sets $\left\{ \Gamma_{C,u} \right\}_{C \in \mathbb{R}}$ in $\mathbb{R}^3$ is independent of the parameter u, in the sense that for any two u_1, u_2 one can find C_1, C_2 such that $\Gamma_{C_1,u_1} = \Gamma_{C_2,u_2}$.*

As will be confirmed later by our numerical tests, when the foliated condition above holds, the directions of propagation associated with the equation (2.10) depend on the spatial variable x only, and are independent on the variable u; hence, the level sets are determined by the spatial variable only and remain unchanged over time, even under the evolution of the solution.

A typical subclass of interest is obtained when h has the following splitting form.

Definition 2.2 *All gradient flux vector field $F(x,u) = n(x) \wedge \nabla_x h(x,u)$ defined on the sphere S^2 and associated with a potential function h of the form*

$$h(x,u) = \overline{h}(x) f(u) \tag{2.15}$$

(for an arbitrary $\overline{h}$) are foliated and are referred to as **foliated flux field based on splitting.**

Flux vectors of the form above will be investigated later in numerical tests. In particular, we use the x**-linear potential functions**, defined by $h(x,u) = (x \cdot a) f(u)$, where a is some constant vector in $\mathbb{R}^3$. In the latter situation, we have a very natural slicing of the sphere S^2 by planes in $\mathbb{R}^3$. In all the above cases, we obtain decoupled "dynamics" on each level set. If the family of level sets is locally a family of curves, then the conservation laws reduces to a family of one-dimensional equations on each curve.

2.3.2 Notion of independent domains

When the flux is *not* foliated, we will consider that we are in a "generic" situation and will use the terminology **"generic flux field"** and, in this case, the potential function $h = h(x,u)$ does not have the specific structure exhibited above. Yet, this function can be decomposed into some homogeneous terms and the evolution of the solution is influenced by all those terms, especially, the direction of propagation changes during the evolution, until the solution finally converges asymptotically to some limiting state.

The following notion of "independent domain" on the sphere, presented now, will be of importance in our forthcoming study of the asymptotic convergence of solutions.

Definition 2.3 *Given a gradient flux field, a subset of the sphere S^2 is called a* **independent domain** *if within the family of level sets $\left\{\Gamma_{C,u}\right\}_{C\in\mathbb{R}}$, one can find one level set that is independent of the parameter u and coincides with the boundary of this domain.*

Such independent domains may exist for foliated flux field as well as generic flux fields. For example, the circle on the sphere defined by $x_1 = 0$ splits the sphere in two independent domains for the foliated flux based on the potential function $h_1(x,u) = x_1 u^2$. The same is true for the generic flux field based on the potential function $h_2(x,u) = x_1 u^2 + x_1 x_2 u^3$.

2.3.3 Genuine nonlinearity and late-time asymptotics

Consider now the dependency of the scalar potential h in u. A special situation is obtained when the function h is linear in u, and in which case we use the terminology **"linear flux".** The classification that we introduced to distinguish between foliated flux and generic flux, and the character of linearity of the flux are expected to be sufficient to predict the late-time asymptotic behavior of the solutions. The following will be validated numerically concernign the asymptotic behavior of solutions. Under the notation and assumptions (2.11) and (2.13) and for any initial condition, three late-time asymptotic behaviors are expected for entropy solutions of equation (2.10):

- For linear foliated flux, the solutions are simply transported within the level sets.
- If the flux is foliated with nonlinear behavior, the solution converges to its constant average in each level set.
- The generic flux generates large variations in solutions, which finally converge to constants within independent domains on the sphere.

The late-time asymptotic behavior of the solutions for linear foliated flux is numerically studied in Section 4 using Test 1-a and Test 1-b. According to our analysis, we concluded that in general for this type of flux, the solution is transported along each level set. The propagation speeds of the solution along the sets depend on the variation of the scalar potential function according to the spatial variable.

We examine the case of nonlinear foliated flux using Test 2-b, Test 3-a and Test 5 presented, respectively in Sections 5, 6 and 8. In general for this type of flux the solution converges to its constant average in each level set as examined in Test 5. Some particular behaviors can be numerically observed according to the structure of the computational grid for nonlinear foliated fluxes in which the solution converges to constant values in independent domains on the sphere. The lines which split these domains are part of the level sets. As examples, the solution of Test 2-b converges asymptotically to two constant values in two independent domains on the sphere and the solution of Test 3-a converges to one constant value on the entire sphere.

For a generic flux, as will be shown by the tests performed in Section 7, the behavior of the solution is largely influenced by the dependency of the scalar potential $h(x, u)$ both on the spatial variable x and the value of the function u. In those tests we consider generic fluxes in which the scalar potential is composed of different homogeneous fluxes. Following the tests performed in this paper, for this type of flux, the solution converges to constant values in independent domains on the sphere. The system of equations is conservative. Thus the constant values, which are the asymptotic limits of convergence, represent the averages of the function taken as initial condition in those domains.

2.4 Special classes of solutions

2.4.1 Wave structure

There are many solutions of particular interest which may have a very rich wave structure, including spatially periodic solutions and steady state solutions. Since for the foliated flux, the system of equations of interest can be reduced to a family of one-dimensional equations on level sets, this type of flux is considered to construct some particular and interesting solutions. The Foliated flux with linear behavior is used to obtain the spatially periodic solutions. The foliated flux with nonlinear behavior is employed to construct large families of stationary solutions which are communally used in the numerical

tests to check the well-balanced property. We will see in our numerical tests that for nonlinear foliated flux, the level sets introduced in this paper can be used to improve the numerical schemes by considering a suitable choice of the mesh in order to preserve the stationary solutions. More precisely, in order to preserve numerically the steady state solutions, the lines of the computational grids should be a part of the level sets and their equipotential curves which are orthogonal to them.

2.4.2 Spherical coordinates

The two-dimensional spherical coordinate system is considered here. The position of each point on the sphere is specified by its longitude $\lambda \in [0, 2\pi]$ and its latitude $\phi \in [-\pi/2, \pi/2]$. The coordinates are singular at the south and north poles, corresponding to $\phi = -\pi/2$ and $\phi = \pi/2$, respectively. The Cartesian coordinates are denoted by $x = (x_1, x_2, x_3) \in \mathbb{R}^3$ with the corresponding standard basis vectors i_1, i_2 and i_3. The spherical coordinates under consideration lead to the following unit normal vector to the sphere.

$$n(x) = \cos\phi\cos\lambda i_1 + \cos\phi\sin\lambda i_2 + \sin\phi i_3,$$

and for each point on the sphere with coordinates (λ, ϕ), we obtain the following unit tangent vectors in the directions of longitude and latitude

$$\begin{aligned} i_\lambda &= -\sin\lambda i_1 + \cos\lambda i_2, \\ i_\phi &= -\sin\phi\cos\lambda i_1 - \sin\phi\sin\lambda i_2 + \cos\phi i_3. \end{aligned}$$

The equation of conservation law (2.10), can be rewritten using the spherical coordinates in the following form:

$$\partial_t u + \frac{1}{\cos\phi}\left(\frac{\partial}{\partial\phi}(F_\phi\cos\phi) + \frac{\partial F_\lambda}{\partial\lambda}\right) = 0, \tag{2.16}$$

where F_λ and F_ϕ are the flux components in spherical coordinates. They are given for each three-dimensional flux of the form $\Phi(x,u) = \hat{f}_1(x,u)i_1 + \hat{f}_2(x,u)i_2 + \hat{f}_3(x,u)i_3$ as follows:

$$\begin{aligned} F(x,u) &= F_\lambda(\lambda,\phi,u)i_\lambda + F_\phi(\lambda,\phi,u)i_\phi, \\ F_\lambda(\lambda,\phi,u) &= \hat{f}_1(x,u)\sin\phi\cos\lambda + \hat{f}_2(x,u)\sin\phi\sin\lambda - \hat{f}_3(x,u)\cos\phi, \\ F_\phi(\lambda,\phi,u) &= -\hat{f}_1(x,u)\sin\lambda + \hat{f}_2(x,u)\cos\lambda. \end{aligned} \tag{2.17}$$

2.4.3 Solutions for linear foliated flux

We consider the family of linear fluxes defined on the basis of the scalar potential $h(x,u) = \overline{h}(x)u$ with $\overline{h}(x) = -cx_3^k$ for an integer $k \geq 1$ and a real number

c chosen arbitrarily. Under these considerations, the three-dimensional flux reads

$$\Phi(x,u) = \nabla_x h(x,u) = -ckx_3^{k-1} u i_3. \tag{2.18}$$

The components of the flux in spherical coordinates can be deduced by using the explicit formulas (2.17) as follows

$$\begin{aligned} F_\lambda(\lambda,\phi,\lambda) &= ckx_3^{k-1}\cos\phi u, \\ F_\phi(\lambda,\phi,\lambda) &= 0. \end{aligned} \tag{2.19}$$

Finally, it is easy to derive the analytical solution for any initial condition $u_0(\lambda,\phi)$

$$\begin{aligned} u(x,t) &= u_0(\lambda - c_\phi^* t, \phi), \\ c_\phi^* &= ckx_3^{k-1}. \end{aligned} \tag{2.20}$$

The level sets of this type of fluxes are the circles on the sphere defined by constant latitudes. For $k = 1$ the solution is simply transported within those level sets with the same angular speed and it is globally preserved in a rotating frame. For $k > 1$ the solution is transported within the level sets with different angular speeds and it is preserved in a moving frame along each level set but the solution is not globally preserved. We note that more general forms of the solutions for linear fluxes can be obtained by considering other functions $\overline{h}(x)$.

2.4.4 Non-trivial steady state solutions

In this section, we present some general classes of non-trivial steady state solutions which will be used in the numerical tests. As mentioned before, foliated fluxes are used to construct non-trivial stationary solutions. More precisely, based on the expected asymptotic behavior for non-linear foliated flux, the solution of the equation (2.10) evolves along each level set and for long time, this solution converges asymptotically to constant value on each level set. Thus, it is straightforward (but fundamental) to deduce that for this type of flux, any stationary solution of the equation (2.10) must be constant along each level set. This result is important and further simplifies the problem to find the stationary solutions. However, for the solutions which are used in our numerical tests, it will be proved that they are stationary. We will be particularly interested, in this section, to a linear splitting flux vector defined on the basis of the scalar potential $h(x,u) = (x.a)f(u)$ for some constant vector $a = a_1 i_1 + a_2 i_2 + a_3 i_3$ in $\mathbb{R}^3$. For this case the corresponding flux is obtained as

$$F(x,u) = f(u)n(x) \wedge a.$$

The level sets of this flux are the circles defined as the intersections of the sphere with the planes defined as $x.a = c$, where $c \in [-\|a\|_2, \|a\|_2]$. These level sets will be parametrized by the real constant c and denoted by Γ_c.The

following Corollary describes for the above-mentioned type of flux, a family of non-trivial steady state solutions

Corollary 2.4 ***(A family of steady sate solutions).*** *Consider the foliated flux vector $F(x,u) = f(u)n(x) \wedge a$, where a is some constant vector in $\mathbb{R}^3$. For any function $\tilde{u}$ which depends on one variable, the function defined as $u_0(x) = \tilde{u}(x.a) = \tilde{u}(a_1x_1 + a_2x_2 + a_3x_3)$ is a stationary solution to the conservation law* (2.10) *associated to the flux $F(x,u)$.*

Proof. In order to prove that the function $u_0(x)$ is a stationary solution we use the claim 3.2 in [4]. To conduct this, we consider the function $H(x) = H_0(a_1x_1+a_2x_2+a_3x_3)$, where $H_0(\mu) = \int_{\mu_0}^{\mu} f(\tilde{u_0}(\mu))d\mu$. It is clear that $h(x,u) = (x.a)f(u)$ is a smooth function in $\mathbb{R}^3$ in particular in a neighborhood of S^2. The following results are obtained

$$\nabla_y h(y, u_0(x))_{|y=x} = (a_1i_1 + a_2i_2 + a_3i_3)f(\tilde{u_0}(a_1x_1 + a_2x_2 + a_3x_3))$$

and $\nabla_y h(y, u_0(x))_{|y=x} = \nabla_x H(x)$. Therefore, all hypothesis of the claim 3.2 in [4] are satisfied. Finally, the function $u_0(x)$ is a stationary solution of the conservation law (2.10). □

Since $u_0(x) = \tilde{u}(x.a)$, then the function u_0 is constant on each level set Γ_c. We are interested in discontinuous solutions. The results of Corollary 2.4 will be used to construct discontinuous stationary solutions for some selected flux vectors. In particular, if the same assumptions of the Corollary 2.4 are considered with $f(u) = u^2/2$, then for any function $\tilde{u}$ which depends on one variable, the function defined as $u_0(x) = \chi(x.a)\tilde{u}(x.a)$ is a stationary solution to the conservation law (2.10), where $\chi(x.a)$ is a discrete function which depends on the variable $x.a$ and has the values of ± 1 .

Particular values of the vector a will be used in order to construct several forms of foliated flux which will be used in the numerical tests. In the second test, we consider the flux of the form $F(x,u) = f(u)n(x) \wedge i_1$ (i.e $a = i_1$). For this flux any function which depends on the first coordinate x_1 only, is a steady state solution of the equation (2.10). In the third test, the vector $a = i_1 + i_2 + i_3$ is considered and for this case we obtain a steady state solution in a spherical cap of the form $u_0(x) = \tilde{u}_0(x_1 + x_2 + x_3)$, where $\tilde{u}_0$ is any real function depending on one variable.

3 Geometric GRP method on the sphere

3.1 Discrete form of the scheme

Following [4], we design a Godunov-type, finite volume scheme that is based on an intrinsic approach and provides an accurate treatment of the geometry. Second-order accuracy is obtained with the technique developed by Ben–Artzi

and Facolvitz [3], LeFloch and Raviart [14], and Bourgeade et al. [7]. Earlier work was done by Berger et al. [6] and Rossmanith [18,19] based on high resolution schemes and approximate Riemann solvers, but by embedding the sphere in a "cubic mesh" in $\mathbb{R}^3$.

In the following, we present the discrete form of the geometry-compatible finite volume scheme which was formulated in [4]. In order to ensure a suitable discrete form, an important condition obtained from the theory established by Ben-Artzi and LeFloch [5] called the "zero-divergence" was used in the construction of the scheme. We provide some details about the discrete form of the divergence operator and the second order method using General Riemann Problem solver (GRP) based on an operator splitting approach. The second order scheme respects the geometry-compatibility condition in the GRP framework and it is used to improve the expected order of accuracy.

The general structures of the cells used in the numerical scheme are shown in Figure 1 and Figure 2. When we go from the equator to the north or south poles, for some special latitude circles, the cell is changed by a ratio of 2 in order to reduce the number of cells, to respect the condition of stability and to have homogeneous precision in the entire domain of the sphere. The domain of each cell is defined as $\Omega := \{\lambda_1 \leqslant \lambda \leqslant \lambda_2, \phi_1 \leqslant \phi \leqslant \phi_2\}$. A cell near the north or south poles has three sides which is a special case of the standard cell shown in Figure 1 with zero length for one side.

In [4], the divergence operator is discretized using the geometry-compatible condition and the flux is approximated by using the following formula:

$$(\nabla_{S^2} \cdot (F(x, u(t, x))))^{approx} = \frac{I_i}{\omega_i}, \tag{3.1}$$

where $I_i = (\oint_{\partial\Omega} F(x,u).\vec{n}ds)^{approx}$, $\vec{n}$ is the unit normal vector to the boundary $\partial\Omega$ of the cell, and ds is the arc length along $\partial\Omega$. The parameter I_i is calculated for each side e of the cell in terms of the scalar potential h using the following expression:

$$\left(\oint_{e_1}^{e_2} F(x,u).\vec{n}ds \right)^{approx} = -(h(e_2, u_m) - h(e_1, u_m)), \tag{3.2}$$

where e_1 and e_2 are, respectively, the initial and final endpoints of the edge e and u_m is the solution of the Riemann problem in the orthogonal direction to the interface e

3.1.1 Equations for the splitting approach

The different approximations used in the numerical scheme are based on the splitting of the equations. Without loss of generality, the following scalar po-

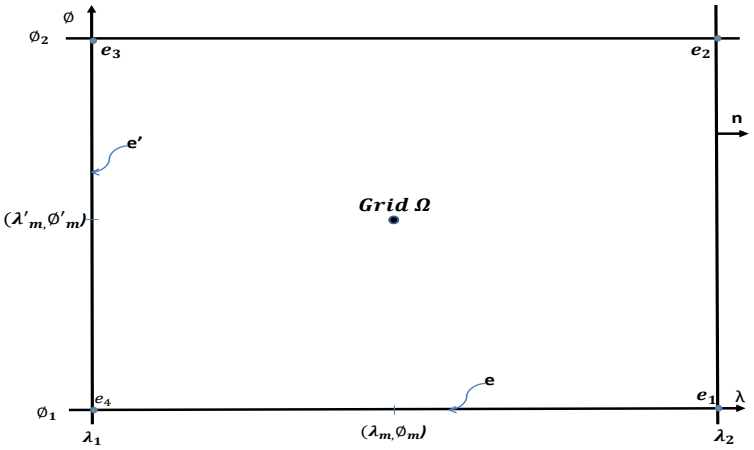

Figure 1. Grid type 1 on S^2.

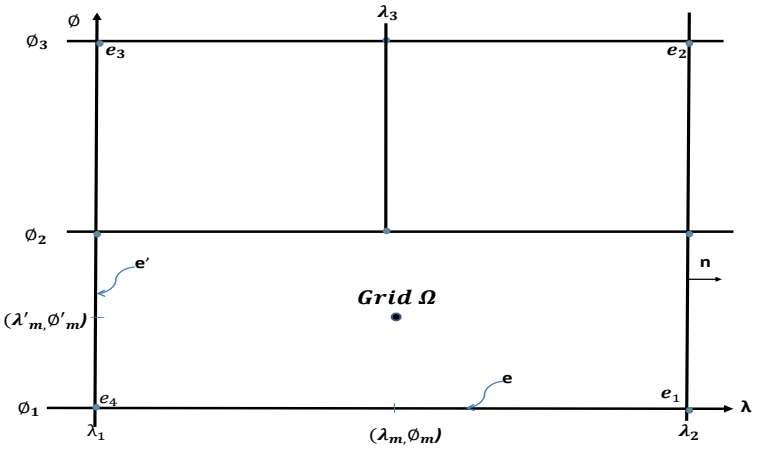

Figure 2. Grid type 2 on S^2.

tentials are used to explain the procedure and the different equations of the splitting approach

$$h(x,u) = h_1(x)f_1(u) + h_2(x)f_2(u) + h_3(x)f_3(u), \tag{3.3}$$

which leads to the corresponding gradient flux vector:

$$\begin{aligned}&\Phi(x,u)\\ &= \nabla_x h(x,u) = \sum_{j=1}^{j=3} \frac{\partial h_j(x)}{\partial x_1} f_j(u) i_1 + \sum_{j=1}^{j=3} \frac{\partial h_j(x)}{\partial x_2} f_j(u) i_2 + \sum_{j=1}^{j=3} \frac{\partial h_j(x)}{\partial x_3} f_j(u) i_3.\end{aligned} \tag{3.4}$$

Using Claim 2.2 in [4], the above expression of $\Phi(x,u)$ as a gradient ensures the validity of the geometry compatibility condition. The equations (2.17) are used to obtain the following flux components in spherical coordinates:

$$\begin{aligned}F_\lambda(\lambda,\phi,u) &= \Phi_1(x,u)\sin\phi\cos\lambda + \Phi_2(x,u)\sin\phi\sin\lambda - \Phi_3(x,u)\cos\phi,\\ F_\phi(\lambda,\phi,u) &= -\Phi_1(x,u)\sin\lambda + \Phi_2(x,u)\cos\lambda,\end{aligned} \tag{3.5}$$

where $\Phi_i(x,u) = \sum_{j=1}^{j=3} \frac{\partial h_j(x)}{\partial x_i} f_j(u), i = 1,2,3.$

The geometry compatibility condition is equivalent to the following relation in spherical coordinates which is valid for any constant value $\bar{u} \in \mathbb{R}$:

$$\frac{\partial F_\phi(\lambda,\phi,\bar{u})\cos(\phi)}{\partial\phi} + \frac{\partial F_\lambda(\lambda,\phi,\bar{u})}{\partial\lambda} = 0. \tag{3.6}$$

Then, we find

$$\begin{aligned}
&-\sin\lambda \sum_{j=1}^{j=3} \frac{\partial h_{j1}^{'}(x)\cos\phi}{\partial\phi} f_j(u) + \cos\lambda \sum_{j=1}^{j=3} \frac{\partial h_{j2}^{'}(x)\ cos\phi}{\partial\phi} f_j(u) \\
&+\sin\phi \sum_{j=1}^{j=3} \frac{\partial h_{j1}^{'}(x)\cos\lambda}{\partial\lambda} f_j(u) \\
&+\sin\phi \sum_{j=1}^{j=3} \frac{\partial h_{j2}^{'}(x)\sin\lambda}{\partial\lambda} f_j(u) - \cos\phi \sum_{j=1}^{j=3} \frac{\partial h_{j3}^{'}(x)}{\partial\lambda} f_j(u) = 0,
\end{aligned} \tag{3.7}$$

where $h_{ji}^{'}(x) = \frac{\partial h_j(x)}{\partial x_i}, \quad i = 1,2,3 \quad j = 1,2,3.$ Using the conservation law in spherical coordinates (2.16), the flux components given by equations (3.5), and the geometry-compatibility property formulated by equation (3.7), we establish the following equivalent formulation of the conservation law, which is easier to work with:

$$\begin{aligned}
&\frac{\partial u}{\partial t} - \sum_{j=1}^{j=3} h_{j1}^{'}(x) \frac{\partial f_j(u)}{\partial\phi} \sin\lambda + \sum_{j=1}^{j=3} h_{j2}^{'}(x) \frac{\partial f_j(u)}{\partial\phi} \cos\lambda \\
&+\tan\phi \Big(\sum_{j=1}^{j=3} h_{j1}^{'}(x) \frac{\partial f_j(u)}{\partial\lambda} \cos\lambda + \sum_{j=1}^{j=3} h_{j2}^{'}(x) \frac{\partial f_j(u)}{\partial\lambda} \sin\lambda\Big) \\
&-\sum_{j=1}^{j=3} h_{j3}^{'}(x) \frac{\partial f_j(u)}{\partial\lambda} = 0.
\end{aligned} \tag{3.8}$$

The longitude and the latitude of the midpoint of the interface are denoted

by λ_m and ϕ_m, respectively: the "λ split" equations read

$$\begin{aligned}
&\frac{\partial u}{\partial t} + \frac{\partial g(x,u)}{\partial \lambda} = S_\lambda, \\
&S_\lambda = \tan\phi_m \left[\sum_{j=1}^{j=3} f_j(u) \frac{\partial (h'_{j1}(x)\cos\lambda)}{\partial \lambda} + \sum_{j=1}^{j=3} f_j(u) \frac{\partial (h'_{j2}(x)\sin\lambda)}{\partial \lambda} \right] \\
&\qquad - \sum_{j=1}^{j=3} f_j(u) \frac{\partial (h'_{j3}(x))}{\partial \lambda} \\
&g(x,u) = \tan\phi_m \left[\sum_{j=1}^{j=3} h'_{j1}(x) f_j(u)\cos\lambda + \sum_{j=1}^{j=3} h'_{j2}(x) f_j(u)\sin\lambda \right] \\
&\qquad\qquad - \sum_{j=1}^{j=3} h'_{j3}(x) f_j(u),
\end{aligned} \tag{3.9}$$

while the "ϕ split" equations are

$$\begin{aligned}
&\frac{\partial u}{\partial t} + \frac{\partial k(x,u)}{\partial \phi} = S_\phi, \\
&S_\phi = -\sum_{j=1}^{j=3} f_j(u)\sin\lambda \frac{\partial h'_{j1}(x)}{\partial \phi} + \sum_{j=1}^{j=3} f_j(u) cos\lambda \frac{\partial h'_{j2}(x)}{\partial \phi}, \\
&k(x,u) = -\sum_{j=1}^{j=3} h'_{j1}(x) f_j(u)\sin\lambda + \sum_{j=1}^{j=3} h'_{j2}(x) f_j(u) cos\lambda.
\end{aligned} \tag{3.10}$$

The right-hand side terms S_λ and S_ϕ of the previous equations are the result of the explicit differentiation of the flux functions $g(x,u)$ and $k(x,u)$.

3.2 Second-order approximations based on the GRP method

We now present the algorithm used for the second-order finite volume method based on generalized Riemann solver. Since the same method is applied for the $\lambda-$ and $\phi-$equations, for simplicity the variable ζ is used to denote the variable λ or ϕ, respectively, if the "λ split" or "ϕ split" is considered. The function $\tilde{g}(x,u)$ is also employed as a notation for both $g(x,u)$ and $k(x,u)$ used in the equations (3.9) and (3.10), respectively. The following general equation is obtained:

$$\frac{\partial u}{\partial t} + \frac{\partial \tilde{g}(x,u)}{\partial \zeta} = S_\zeta. \tag{3.11}$$

The right hand side term S_ζ is the result of the differentiation of the function $\tilde{g}(x,u)$ corresponding to case $\zeta = \lambda$ or $\zeta = \phi$ developed in the previous section. In the second order method based on the General Riemann Problem, it is assumed that for any time step t_n, the solution is approximated by a

piecewise linear function. The constant values u_i^n at the cell centers are used to obtain piecewise linear functions $u_i^n(\zeta)$ inside each cell i. This reconstruction leads to the following local function:

$$u_i^n(\zeta) = u_i^n + (\zeta - \zeta_i)s_i^n, \qquad \zeta \in [0, \Delta\zeta], \tag{3.12}$$

where s_i^n are the slopes. The Godunov scheme is the special case of this method by considering $s_i^n = 0$ for all cells. The following extreme values are used to solve the Riemann problem at the interface:

$$u_i^L = u_i^n - \frac{1}{2}\Delta\zeta s_i^n, \quad u_i^R = u_i^n + \frac{1}{2}\Delta\zeta s_i^n. \tag{3.13}$$

The new slope s_i^{n+1} is obtained by using the following steps:

$$\begin{aligned} u_{i+\frac{1}{2}}^{n+1} &= u_{i+\frac{1}{2}}^n + (\frac{\partial u}{\partial t})_{i+\frac{1}{2}}^n (t_{n+1} - t_n), \\ \tilde{s}_i^{n+1} &= \frac{1}{\Delta\zeta}(u_{i+\frac{1}{2}}^{n+1} - u_{i-\frac{1}{2}}^{n+1}), \\ s_i^{n+1} &= \frac{1}{\Delta\zeta}\ minmod((u_{i+1}^{n+1} - u_i^{n+1}), \Delta\zeta\tilde{s}_i^{n+1}, (u_i^{n+1} - u_{i-1}^{n+1})), \end{aligned} \tag{3.14}$$

where the *minmod* function is

$$\begin{aligned} &minmod(\sigma_1, \sigma_2, \sigma_3) \\ &= \begin{cases} \sigma \min(|\sigma_1|, |\sigma_2|, |\sigma_3|), & if\ \sigma = sign(\sigma_1) = sign(\sigma_2) = sign(\sigma_3), \\ 0, & \text{otherwise.} \end{cases} . \end{aligned} \tag{3.15}$$

Subject to the initial data for u, its boundary values denoted by u_L and u_R and its ζ-slope denoted by $u_{L,\zeta}$ and $u_{R,\zeta}$ are used to obtain the solution $\tilde{u}^m$ of the Riemann problem. The General Riemann problem method uses a linear temporal approximation of the value of u^m. The new value is obtained as:

$$u^m = \tilde{u}^m + \frac{\partial u}{\partial t}(\lambda_m, \phi_m, t_n)\frac{\Delta t}{2}. \tag{3.16}$$

In equation (3.16), the derivative term is obtained by using the slope value of u

$$\frac{\partial u}{\partial t}(\lambda_m, \phi_m, t_n) = -u_{m,\zeta}\frac{\partial \tilde{g}(x,u)}{\partial u}\ |_{(\lambda_m, \phi_m, u^m)}\ . \tag{3.17}$$

The parameter $u_{m,\zeta}$ is obtained by the associated Riemann Problem. In the following we recall briefly the procedure used to solve the Riemann problem for u and its slopes. For $u_L \leq u_R$, we consider the "convex envelope" of $\tilde{g}$ and the solution u^m and $u_{m,\zeta}$ are obtained as follows:

$$u^m = arg_{v\in[u_L,u_R]} min(\tilde{g}(x,v) \mid (\lambda_m, \phi_m)). \tag{3.18}$$

To evaluate the parameters u^m and $u_{m,\zeta}$, there are three cases:

(i) A wave moving to the right:

$$u^m = u_L, \qquad u_{m,\zeta} = u_{L,\zeta}. \tag{3.19}$$

(ii) A wave moving to the left:

$$u^m = u_R, \qquad u_{m,\zeta} = u_{R,\zeta}. \tag{3.20}$$

(iii) A sonic point:

$$u_L < u^m < u_R, \qquad \partial_u \tilde{g}(x,u) \mid_{(\lambda_m,\phi_m,u^m)} = 0. \tag{3.21}$$

Not that for the sonic case, it is easy to conclude, using the equations (3.17) and (3.21), that the time-derivative of u reduces to $\frac{\partial u}{\partial t}(\lambda_m, \phi_m, t_n) = 0$. The geometry-compatibility condition remains valid also for the second order scheme. Indeed, if we consider the condition $u \equiv const$ in the computational cell and its neighbors, the slopes and the time-derivatives of the solution in the GRP vanish and the solution remains constant. Finally, under the condition $u_L > u_R$, the same procedure is used by considering the "concave envelope" of $\tilde{g}$ and the value that maximizes the function $\tilde{g}(x,v)$ in the equation (3.18) with $v \in [u_R, u_L]$.

4 First test case with linear foliated flux

Referring to Section 2.4.3, here we perform two tests cases using linear fluxes based on different scalar potentials $h(x,u) = \overline{h}(x)u$. We consider a grid with an equatorial longitude step $\Delta\lambda = \pi/96$ and a latitude step $\Delta\phi = \pi/96$, and a time step $\Delta t = 0.01$. In the first numerical test (Test 1-a), the function $\overline{h}(x) = -x_3$ is considered, which leads to the following flux vector:

$$F_\lambda(\lambda,\phi,\lambda) = \cos\phi u, \qquad F_\phi(\lambda,\phi,\lambda) = 0. \tag{4.1}$$

We consider the initial function with a discontinuity along the curve $x_1 = 0$, defined as:

$$u(0,x) = \begin{cases} \cos\phi, & x_1 \geq 0, \\ -\cos\phi, & \text{otherwise.} \end{cases} \tag{4.2}$$

For this case, the solution is transported with the same angular speed along the level sets which are the circles defined by $\phi = \phi_c$, where $\phi_c \in [-\frac{\pi}{2}, \frac{\pi}{2}]$. Figure 3 shows the solution at time $t = 50$ and confirms that it is globally preserved in rotating frame on the sphere.

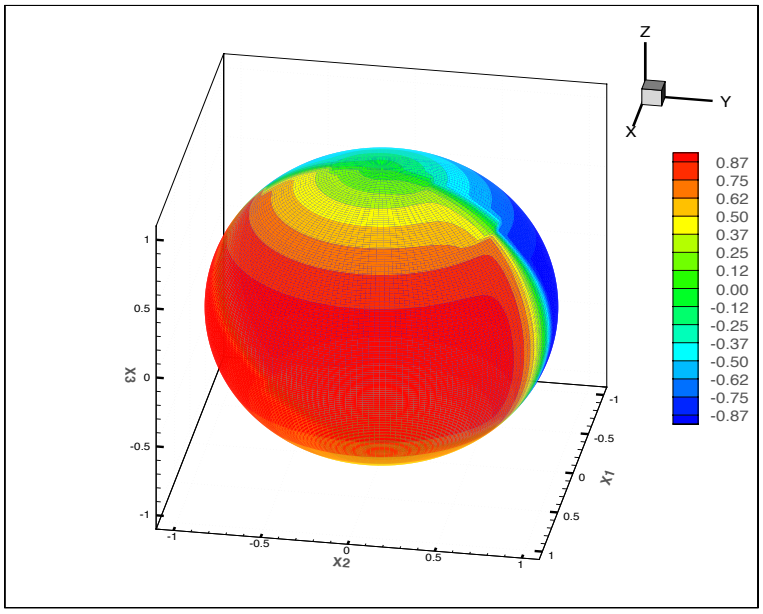

Figure 3. Test 1-a: time $t = 50$ with $\Delta t = 0.01$, $\Delta\lambda = \pi/96$, and $\Delta\phi = \pi/96$.

Now we consider the second test (test 1-b) in which the flux vector is defined on the basis of the scalar potential $h(x, u) = -x_3^2 u$, and the same initial condition is used as the first test. For this test, again the solution is transported along the same level sets but with different angular speeds. As shown in Figure 4 for $t = 50$, the solution is preserved on each level set in a moving frame but not globally preserved on the sphere.

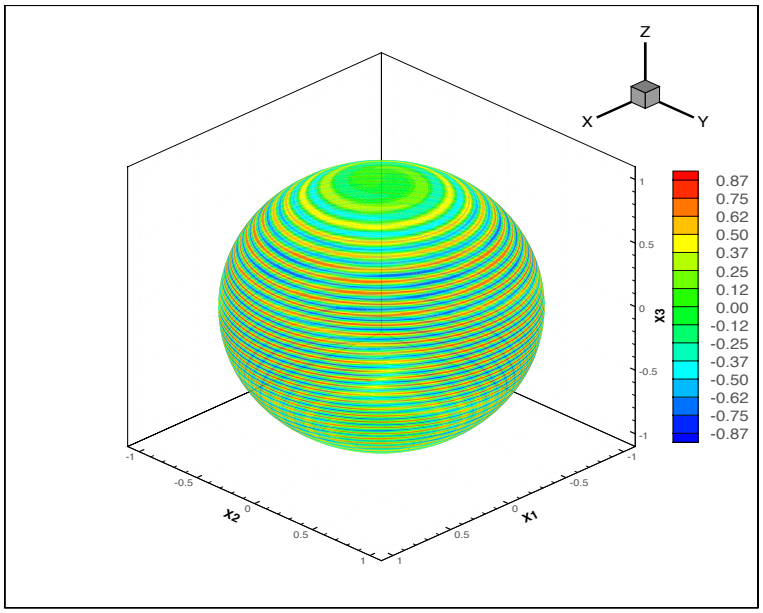

Figure 4. Test 1-b: time $t = 50$ with $\Delta t = 0.01$, $\Delta\lambda = \pi/96$, and $\Delta\phi = \pi/96$.

5 Second test case with nonlinear foliated fluxes

In this section several aspects will be analyzed for nonlinear foliated flux of the form $F(x,u) = f(u)n(x)\wedge i_1$ with $f(u) = u^2/2$. The evolution of L^1 error of the second order scheme is analyzed using discontinuous steady state solutions. The entropy stability property 1.3, the time-variation diminishing property 1.4 and the contraction property 1.5 are analyzed for the first and second order of the scheme. The late-time asymptotic behaviors of the solutions are analyzed using this flux and different initial conditions.

First, we consider the following discontinuous steady state solution of the equation (2.10) which is taken as initial condition (test 2-a).

$$u_1(0,x) = \begin{cases} 1, & x_1 \leq 0, \\ -1, & \text{otherwise.} \end{cases} \tag{5.1}$$

In this test we compute the numerical solution by using the computational cell with equatorial longitude step $\Delta\lambda = \pi/96$ and latitude step $\Delta\phi = \pi/96$, and a time step $\Delta t = 0.01$. Figure 5 shows the numerical solution and the initial condition on the equator of the sphere ($\phi = 0$) at time $t = 100$. As shown in this figure, the numerical solution is in good agreement with the initial condition and it remains steady state.

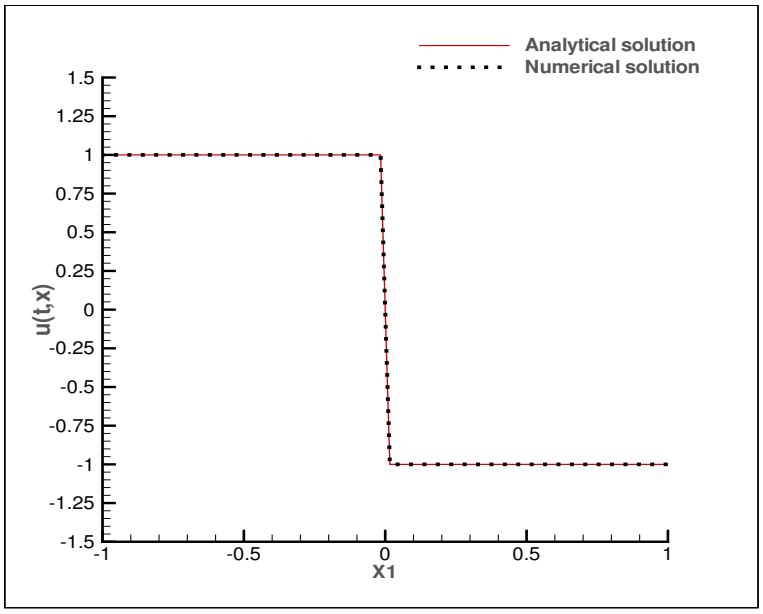

Figure 5. Test 2-a on the equator of the sphere at time $t = 100$ with $\Delta t = 0.01$, $\Delta\lambda = \pi/96$, and $\Delta\phi = \pi/96$.

Finally, a two-dimensional view of the solution at time $t = 100$ is presented in Figure 6 which confirms that the solution remains unchanged over the entire sphere. For this example, since the discontinuity coincide with the level set

$(x_1 = 0)$, there is no numerical impact of the mesh structure on the solution which is preserved for large simulation time. More generally, if we use the assumption that the sides of the mesh coincide with the level sets of the flux and their orthogonal equipotential curves, the second order scheme based on the geometric-compatible property can correctly compute the discontinuous steady sate solutions based on constant values on partially closed domains on the sphere. One can say that the scheme satisfies the discontinuous geometric-compatible property since it is capable to capture all discontinuous steady sate solution based on constant values on closed domains which form a partition on the sphere. But this property is numerically valid if a subset of the level sets is taken as a lines of computational cells which is very important for the performance of the numerical schemes in the case of nonlinear foliated flux.

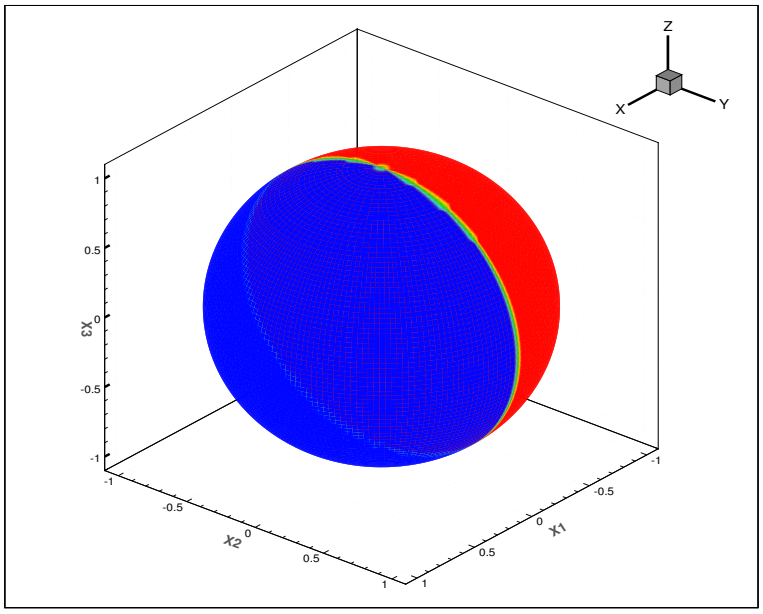

Figure 6. Test 2-a on the entire sphere at time $t = 100$ with $\Delta t = 0.01$, $\Delta\lambda = \pi/96$, and $\Delta\phi = \pi/96$.

Now we consider a Test 2-b using another form of steady state solution, with more discontinuities, which is defined in three domains separated by two closed curves on the sphere defining these discontinuities. The numerical solution is computed by using the same computational grid and time step such as those considered in the previous test.

$$u_2(x) = \begin{cases} x_1^3, & -1 \leq x_1 \leq -0.5, \\ 0.5x_1^2, & -0.5 < x_1 < 0.5, \\ -0.25x_1, & 0.5 \leq x_1 \leq 1. \end{cases} \tag{5.2}$$

Figure 7 shows the numerical solution and the initial condition on the equator of the sphere at time $t = 5$ and Figure 8 shows the two-dimensional view of

the solution at this time on the entire sphere. Accurate results are obtained but for large simulation time, following the comparison between the results of this test to those of test 2-a, we conclude that the numerical scheme is more accurate for the discontinuous steady state solutions based on constants values than for general steady state solutions. This can be justified by the fact that the scheme is based on the geometric compatibility condition which ensures that the constant functions are perfectly preserved by the scheme.

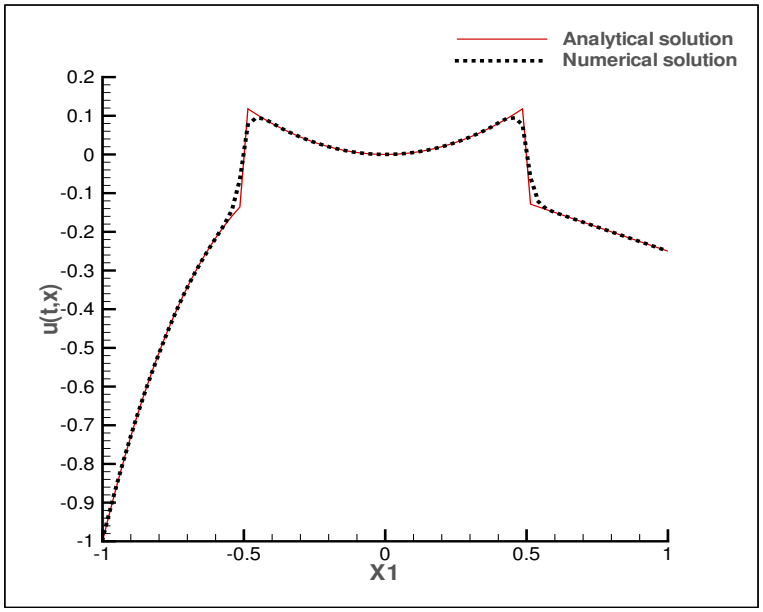

Figure 7. Test 2.b at time $t = 5$ with $\Delta t = 0.01$, $\Delta\lambda = \pi/96$, and $\Delta\phi = \pi/96$.

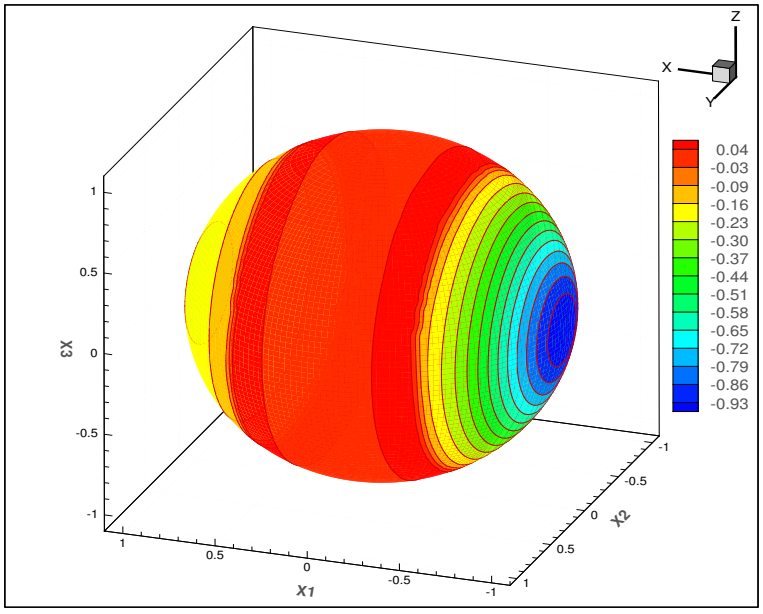

Figure 8. Test 2.b on the entire sphere at time $t = 5$ with $\Delta t = 0.01$, $\Delta\lambda = \pi/96$, and $\Delta\phi = \pi/96$.

Figure 9 shows the evolution of L^1 error of the solution until $t = 100$ and confirms that we obtain accurate results, but for the case of large simulation times the numerical solution is influenced by the mesh structure. It is extremely important to note that in general for nonlinear foliated flux the scheme can preserve the nontrivial stationary solutions with more accurately if the lines of the mesh are part of the level sets of the flux and their orthogonal equipotential curves

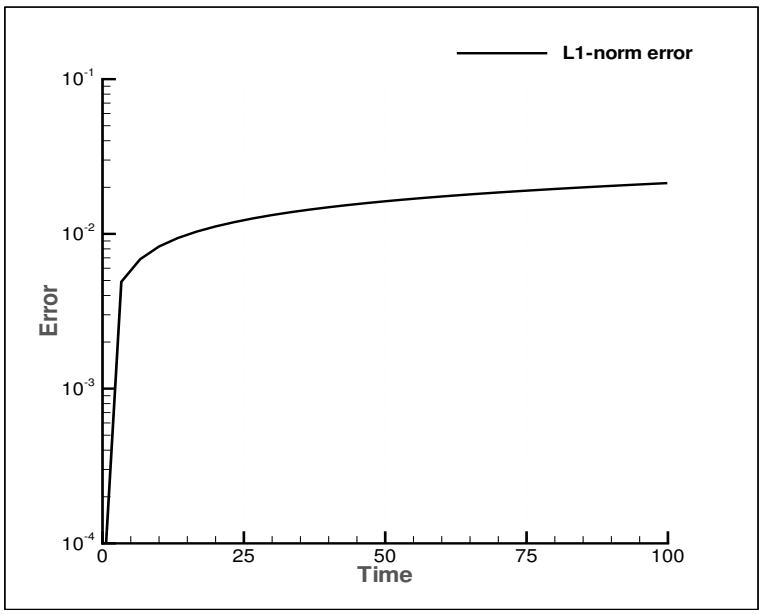

Figure 9. L^1 error for Test 2.b at time $t = 100$ with $\Delta t = 0.01$, $\Delta\lambda = \pi/96$, and $\Delta\phi = \pi/96$.

According to the scalar potential $h(x, u) = x_1 u^2/2$, the circle defined on the sphere by $x_1 = 0$ splits the sphere into two independent domains, the first domain includes the points with $x_1 \geq 0$ and the second includes the points with $x_1 < 0$. The average values of the initial condition in the first and second domains are denoted by $\bar{u_I}$ and $\bar{u_{II}}$, respectively. Figures 10 and 11 show that the parameters $\|u(t) - \bar{u_I}\|_{L^1}$ and $\|u(t) - \bar{u_{II}}\|_{L^1}$ in the first domain and in the second domain of the sphere, respectively, are decreasing over time and tend to zero for large simulation time. The solution converges asymptotically to different constant values in those domains and the convergence is faster in the second domain than the first domain.

Figure 12 presents the two-dimensional view of the solution for a large simulation time and shows that the solution has almost reached to an asymptotic convergence.

Figure 13 shows the evolution of the parameter $\|u(t)\|_{L^p_\omega(M)}$ using L^p norm for $p = 1, 2, 3, 4, 5, 10$ and ∞, and confirms that the entropy stability property 1.3 is checked for all those norms.

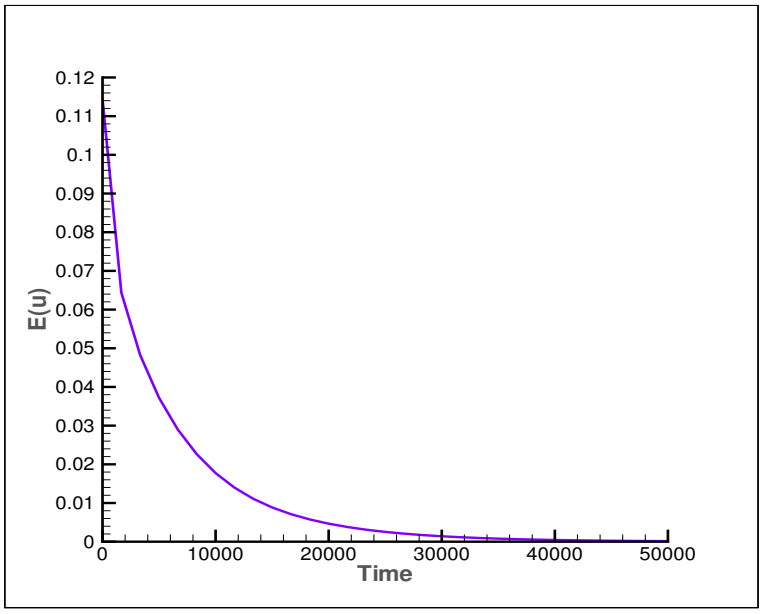

Figure 10. Convergence for Test 2-b: Evolution of the parameter $E(u) = \|u(t) - \bar{u_I}\|_{L^1}$ in domain 1 with $\Delta t = 0.05$, $\Delta\lambda = \pi/96$ and $\Delta\phi = \pi/96$.

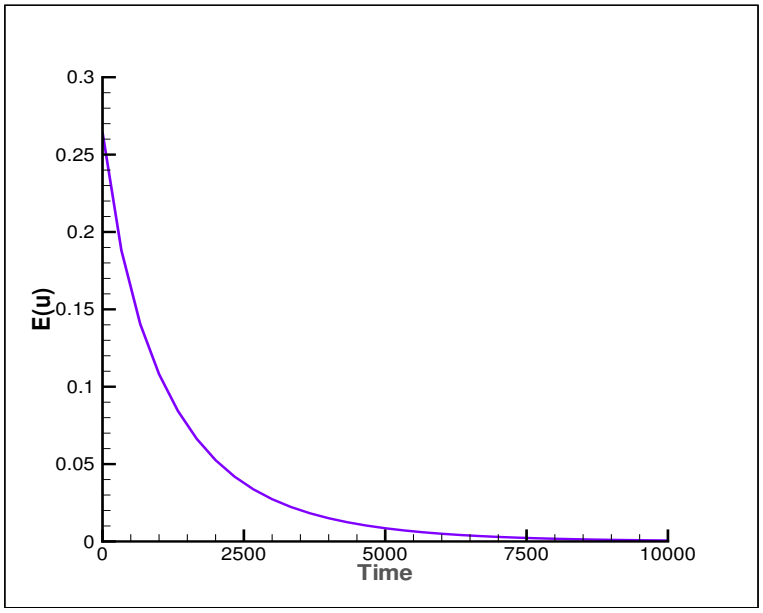

Figure 11. Convergence for Test 2-b: Evolution of the parameter $E(u) = \|u(t) - \bar{u_{II}}\|_{L^1}$ in domain 2 with $\Delta t = 0.05$, $\Delta\lambda = \pi/96$ and $\Delta\phi = \pi/96$.

In the following, the time-variation diminishing property 1.4 is checked for the first and second order forms of the scheme using several initial conditions. Figure 14 confirms that this property is checked for the second order scheme when the function of Test 2-b is used.

Several tests were performed using the following functions in order to verify the time-variation diminishing property 1.4. As shown in Figures 15 and 16,

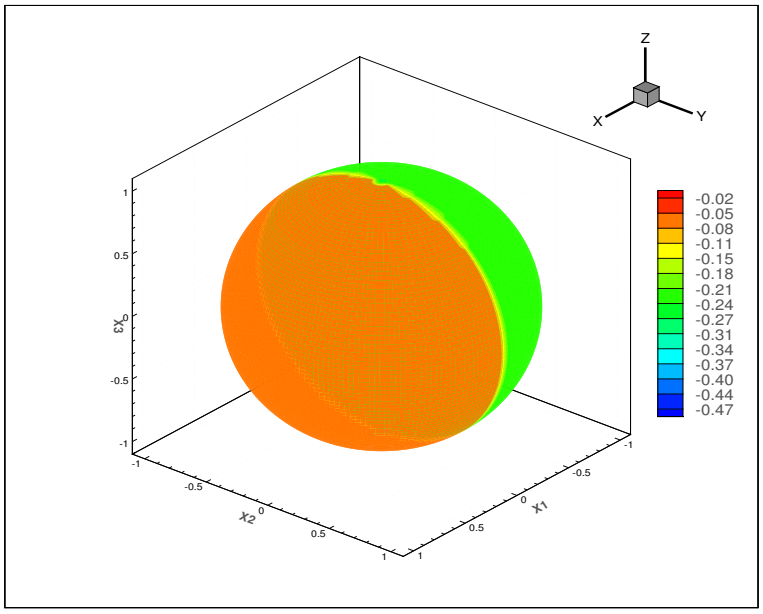

Figure 12. Convergence ofor Test 2-b. Two-dimensional view of the solution at time $t = 50000$ with $\Delta t = 0.05$, $\Delta\lambda = \pi/96$ and $\Delta\phi = \pi/96$.

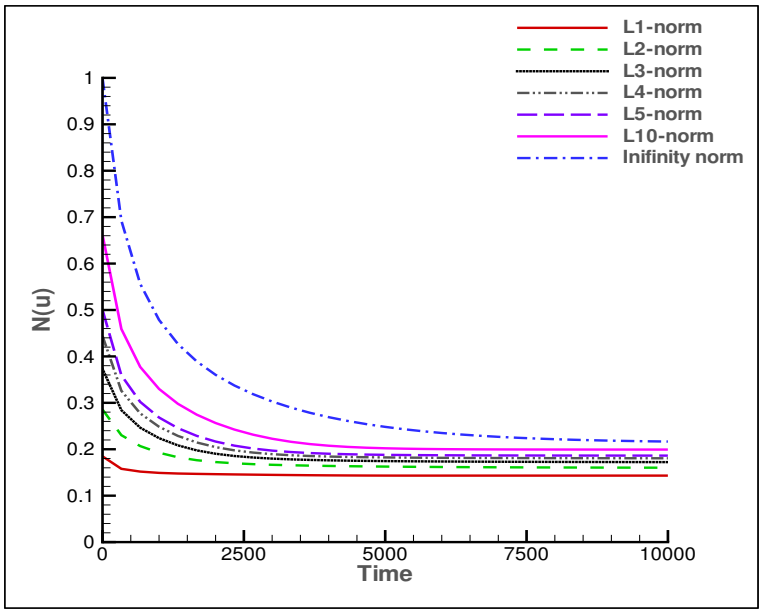

Figure 13. Entropy stability property 1.3 for Test $2-b$ at time $t = 100$ with $\Delta t = 0.01$, $\Delta\lambda = \pi/96$ and $\Delta\phi = \pi/96$.

this property holds for both cases of the first and second order of the scheme.

$$u_1(0,x) = \begin{cases} \sin\lambda, & x_1 \geq 0, \\ -\sin\lambda, & \text{otherwise.} \end{cases} \tag{5.3}$$

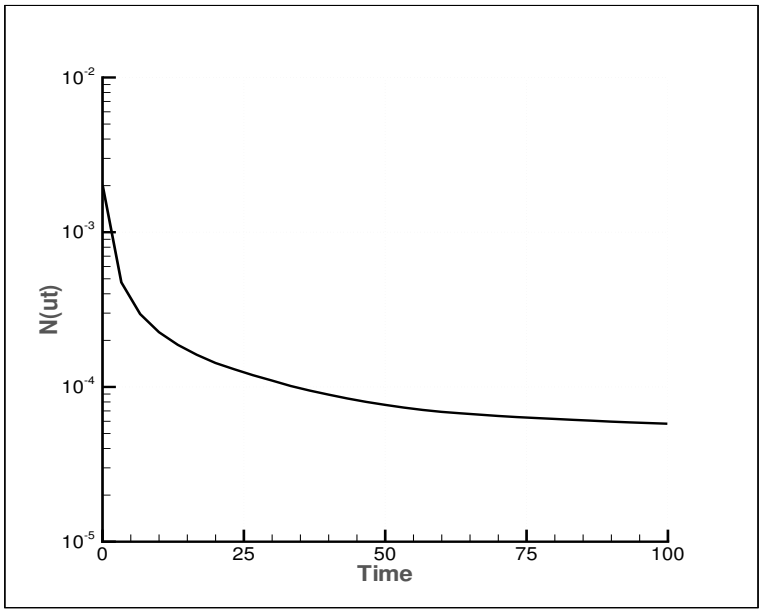

Figure 14. Time-variation diminishing property 1.4 for Test $2-b$ at time $t=100$ with $\Delta t=0.01$, $\Delta\lambda=\pi/96$ and $\Delta\phi=\pi/96$.

$$u_2(0,x)=\begin{cases} x_3, & \lambda\leq\pi,\\ x_3\cos\lambda, & \text{otherwise.}\end{cases} \tag{5.4}$$

$$u_3(0,x)=\begin{cases} x_2, & x_1\leq 0,\\ -x_2e^{x_1}, & \text{otherwise.}\end{cases} \tag{5.5}$$

$$u_4(0,x)=\begin{cases} \frac{1}{\theta-1}, & \theta<0,\\ \frac{1}{1+\theta^2}, & 0\leq\theta\leq 2/\sqrt{3},\\ -3/7, & \text{otherwise.}\end{cases} \tag{5.6}$$

where $\theta=x_1+2x_2+x_3$.

We now proceed to the analysis of the contraction property 1.5 for the the numerical scheme using L^1 norm. We start by giving an example of two functions which verify the contraction property for the first-order scheme but they do not verify this property for the second-order method. We consider the functions v_1 and w_1 defined as:

$$\begin{aligned} v_1(0,x)&=\begin{cases} x_1+x_3^2, & x_1>0,\\ -x_1-x_3^2, & \text{otherwise.}\end{cases}\\ w_1(0,x)&=|x_1|.\end{aligned} \tag{5.7}$$

Figure 17 shows the evolution of the ratio $E(u,v)$ defined by the following formula and confirms that this parameter is decreasing only in the case of the first-order scheme. Then the contraction property 1.5 is valid only for the case

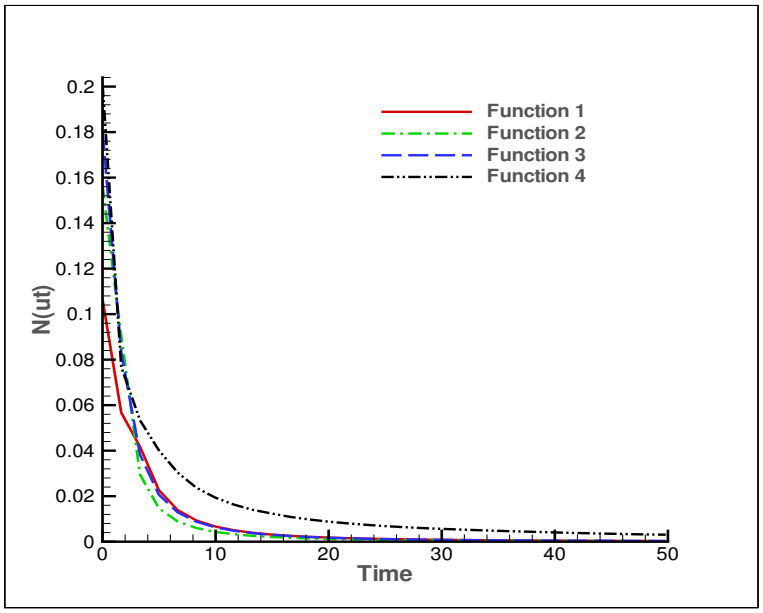

Figure 15. Time-variation diminishing property 1.4 for the first order scheme until time $t = 50$ with $\Delta t = 0.01$, $\Delta\lambda = \pi/96$ and $\Delta\phi = \pi/96$.

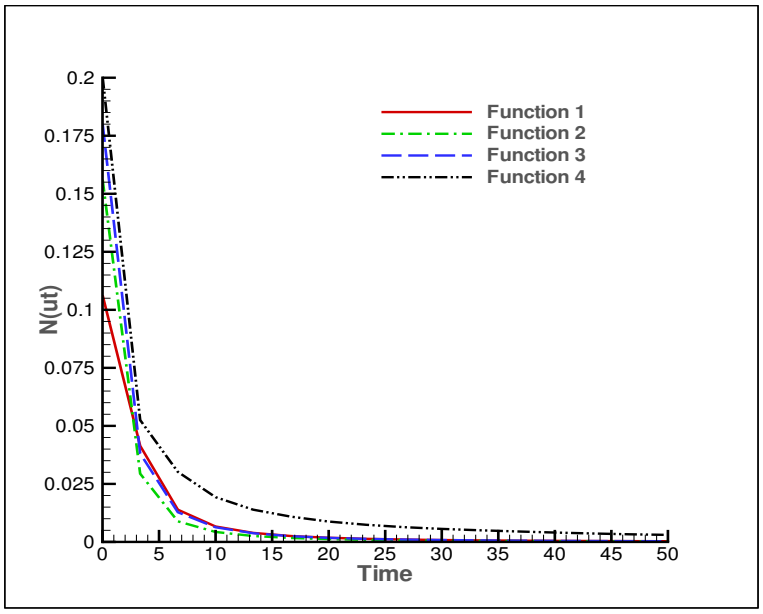

Figure 16. Time-variation diminishing property 1.4 for the second order scheme until time $t = 50$ with $\Delta t = 0.01$, $\Delta\lambda = \pi/96$ and $\Delta\phi = \pi/96$.

of the first-order scheme.

$$E(v, w) = \|v_1(t) - w_1(t)\|_{L^1_\omega(M)} / \|v_1(0) - w_1(0)\|_{L^1_\omega(M)}. \tag{5.8}$$

Several tests are performed to verify the contraction property 1.5 for the first-

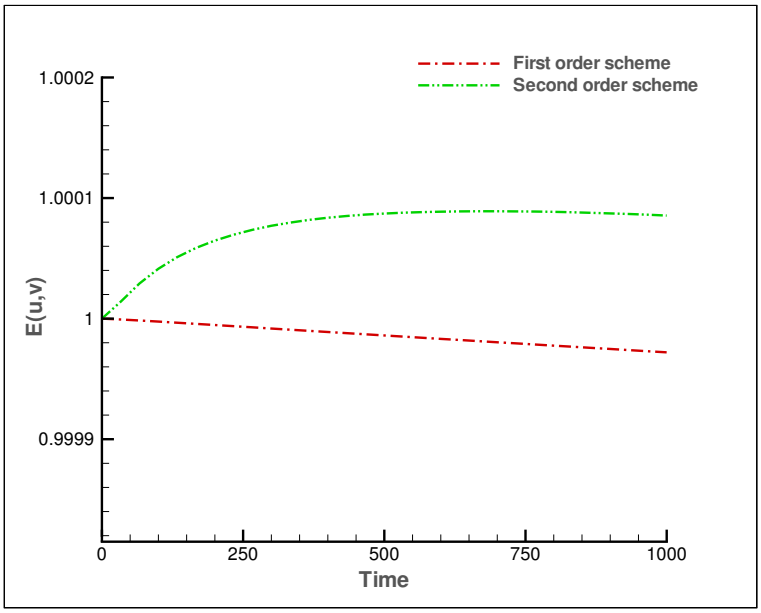

Figure 17. Contraction property 1.5 for the case of first and second order schemes using the L^1 norm with $\Delta t = 0.01$, $\Delta\lambda = \pi/96$ and $\Delta\phi = \pi/96$.

order scheme using the following five pairs of functions.

$$v_1(0,x) = \begin{cases} \sinh(x_1)x_2 - x_3\cosh(x_1), & x_1 \le 0, \\ x_3 + x_1, & \text{otherwise.} \end{cases}$$
$$w_1(0,x) = \begin{cases} x_2x_1^3 + e^{x_1}, & x_1 \le 0, \\ -\cos(x_1) + x_3^2x_1, & \text{otherwise.} \end{cases} \tag{5.9}$$

$$v_2(0,x) = \begin{cases} x_2\cos(x_1), & x_1 \le 0, \\ -x_2, & \text{otherwise.} \end{cases}$$
$$w_2(0,x) = \begin{cases} x_3\cos(x_1), & x_1 \le 0, \\ -x_3 + x_3x_1\log(x_1), & \text{otherwise.} \end{cases} \tag{5.10}$$

$$v_3(0,x) = \begin{cases} x_3^2\cos(\pi x_1) + x_2, & x_1 \le 1/2, \\ -x_2 + x_3(2x_1^2 - x_1), & \text{otherwise.} \end{cases}$$
$$w_3(0,x) = \begin{cases} x_2x_3\cos(\pi x_1) + x_3(x_1^4 - x_1), & x_1 \le 1, \\ x_2x_3, & \text{otherwise.} \end{cases} \tag{5.11}$$

$$v_4(0,x) = \begin{cases} x_2e^{x_1+x_3}, & x_1 \le 0, \\ -x_2e^{x_3}, & \text{otherwise.} \end{cases}$$
$$w_4(0,x) = \begin{cases} \frac{x_2x_3}{1-x_1}, & x_1 \le 0, \\ x_1^2 - x_2x_3, & \text{otherwise.} \end{cases} \tag{5.12}$$

$$v_5(0,x) = \begin{cases} \cosh(x_1+x_2), & x_1 \le 0, \\ -\cosh(x_2), & \text{otherwise.} \end{cases}$$
$$w_5(0,x) = \begin{cases} \cosh(x_3), & x_1 \le 0, \\ -\cosh(x_3), & \text{otherwise.} \end{cases} \tag{5.13}$$

Figure 18 shows the evolution of the ratio $E(u,v)$ for the five pairs of functions. This parameter is decreasing for all cases, which confirms that the contraction property 1.5 is valid for all pairs of functions considered.

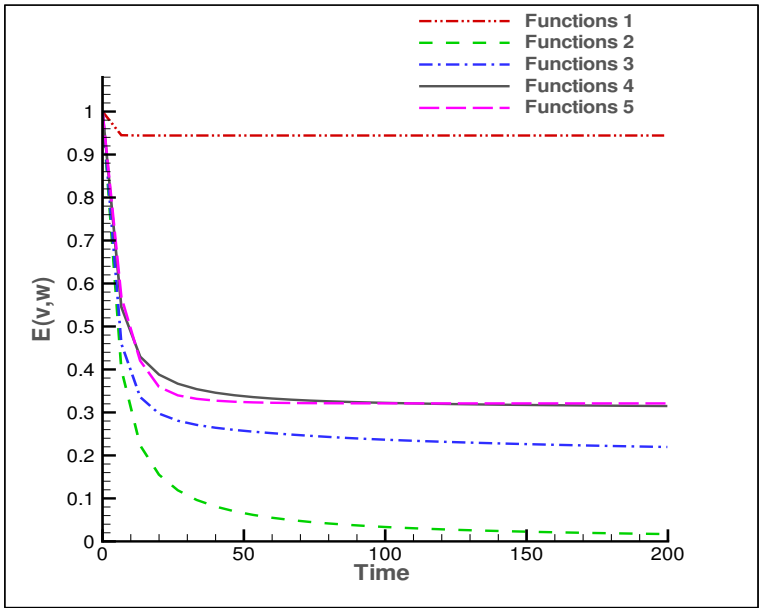

Figure 18. Contraction property 1.5 for the first odrer scheme with $\Delta t = 0.01$, $\Delta\lambda = \pi/96$ and $\Delta\phi = \pi/96$.

6 Third test case with nonlinear foliated fluxes –an alternative form

We consider the nonlinear foliated flux defined in Section 2 of the form $F(x,u) = f(u)n(x)\wedge(i_1+i_2+i_3)$ which corresponds to the scalar potential $h(x,u) = (x_1+x_2+x_3)f(u)$. For this flux, any function of the form $u_0(x) = \tilde{u}_0(x_1+x_2+x_3)$ is a steady state solution of the equations (2.10). In this section the tests are performed using $f(u) = u^2/2$. We consider the following discontinuous steady state solution:

$$u_1(0,x) = \begin{cases} \frac{\theta^3+1}{5-\theta}, & -\sqrt{3} \le \theta \le 0, \\ \theta^2 - \theta - 1/5, & \text{otherwise.} \end{cases} \tag{6.1}$$

where $\theta = x_1 + x_2 + x_3$. Using the inequality $(x_1 + x_2 + x_3)^2 \leq 3(x_1^2 + x_2^2 + x_3^2)$ we obtain $\theta \in [-\sqrt{3}, \sqrt{3}]$.

The present test (3-a) is performed with the above function as initial condition, using a grid with equatorial longitude step $\Delta\lambda = \pi/96$ and latitude step $\Delta\phi = \pi/96$, and a time step $\Delta t = 0.01$. Figures 19 and 20 show the comparison between the numerical solution at time $t = 5$ and the initial condition on the equator of the entire sphere for $0 \leq \lambda \leq \pi$ and $\pi \leq \lambda \leq 2\pi$, respectively. Figure 21 shows a two-dimensional view of the solution on the sphere at time $t = 5$. According to those figures, one can conclude that the second order scheme leads to good results for $t = 5$.

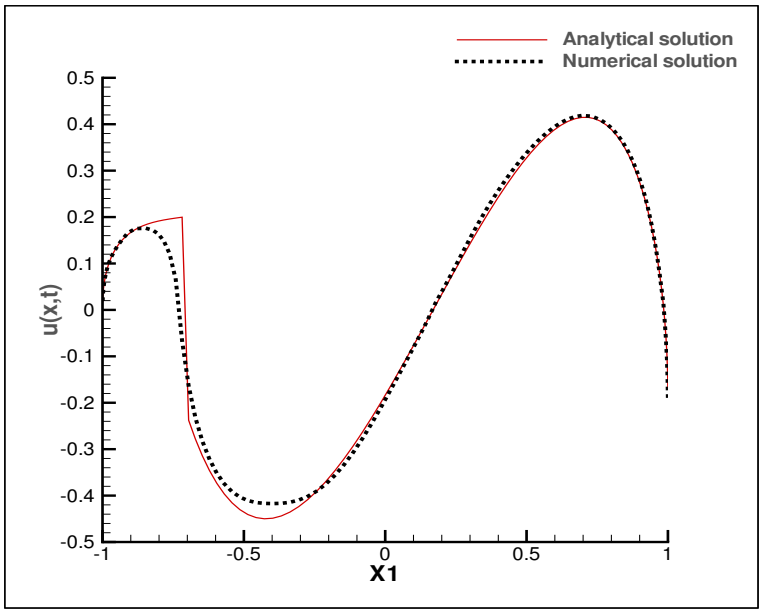

Figure 19. Test 3-a on the equator of the sphere with $0 \leq \lambda \leq \pi$ at time $t = 5$ with $\Delta t = 0.01$, $\Delta\lambda = \pi/96$ and $\Delta\phi = \pi/96$.

The evolution of L^1 error of the solution is presented in Figure 22 until $t = 100$ and again for this case the solution is influenced by the mesh structure. Figure 23 shows the evolution of the parameter $\|u_1(t) - \bar{u_1}\|_{L^1}$, where $\bar{u_1}$ is the average value of the solution on the sphere. For large simulation time, the solution converges to constant value in the entire sphere.

The entropy stability property 1.3 is analyzed using the entropy solution (6.1) with the L^p norm for $p = 1, 2, 3, 4, 5, 10$ and ∞. As shown in Figure 24, this property is checked for all those norms.

The the time-variation diminishing property 1.4 is now checked for the first

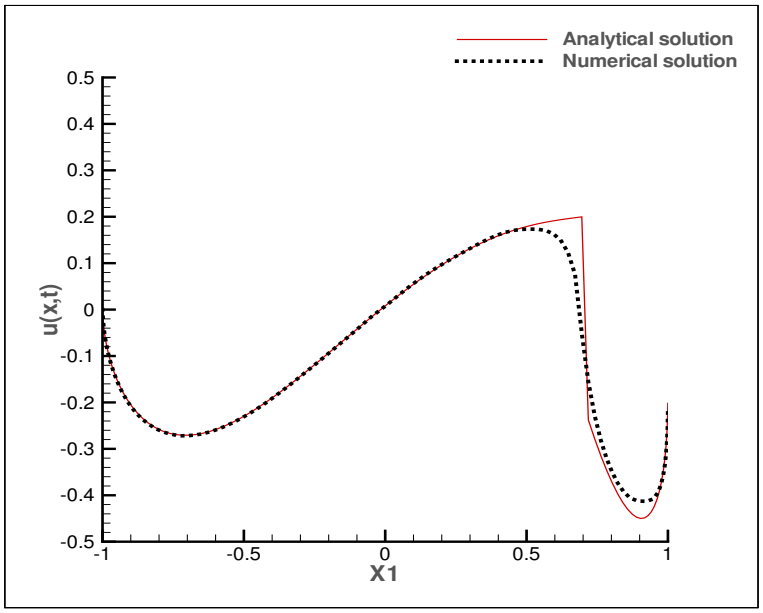

Figure 20. Test 3-a on the equator of the sphere with $\pi \leq \lambda \leq 2\pi$ at time $t = 5$ with $\Delta t = 0.01$, $\Delta\lambda = \pi/96$ and $\Delta\phi = \pi/96$.

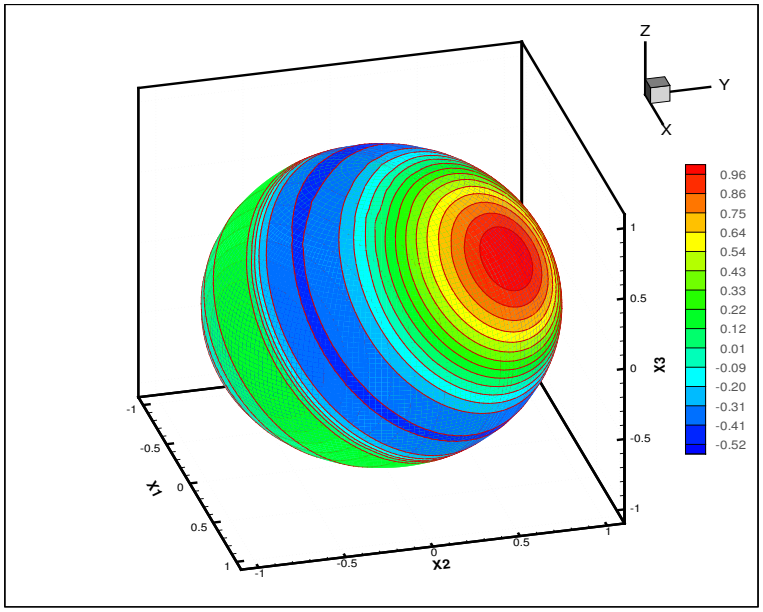

Figure 21. STest 3-a at time $t = 5$ with $\Delta t = 0.01$, $\Delta\lambda = \pi/96$ and $\Delta\phi = \pi/96$.

and second order schemes using the L^1 norm and the following functions:

$$u_1(0,x) = \begin{cases} x_2 + \theta x_1, & -\sqrt{3} \leq \theta \leq 0, \\ -x_2 + \theta x_3, & \text{otherwise.} \end{cases}$$

$$u_2(0,x) = \begin{cases} x_1 + x_2\cos(\lambda), & 0 \leq \lambda \leq \pi/2, \\ -x_1, & \pi/2 < \lambda < \pi, \\ x_1 + x_3\sin(\lambda), & \text{otherwise.} \end{cases} \tag{6.2}$$

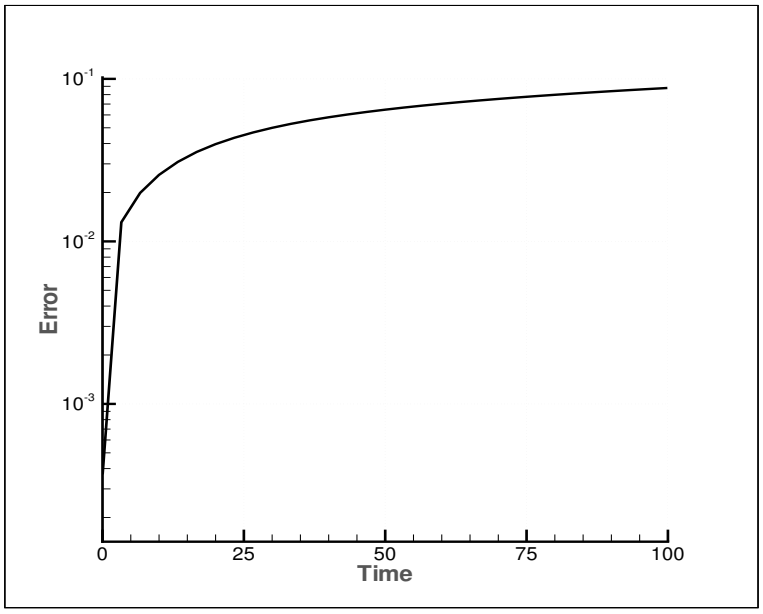

Figure 22. L^1 error for Test 3-a at time $t = 100$ with $\Delta t = 0.01$, $\Delta\lambda = \pi/96$ and $\Delta\phi = \pi/96$.

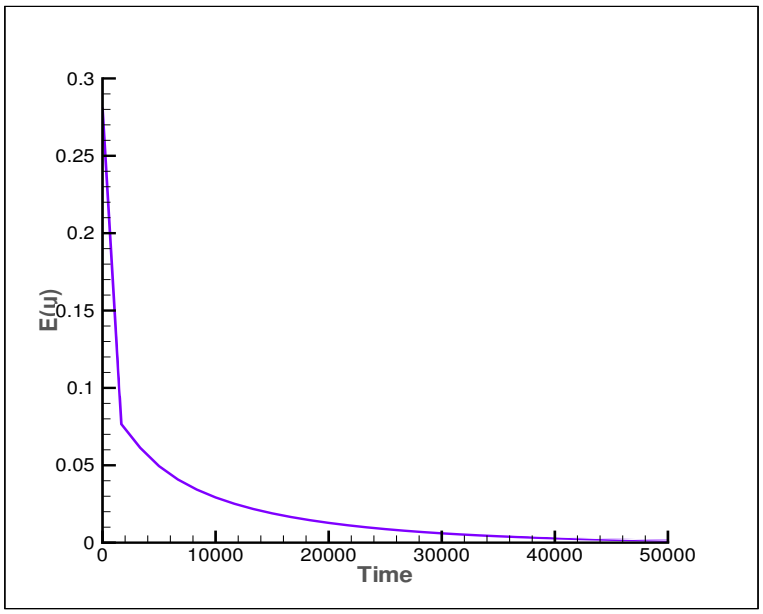

Figure 23. Convergence for Test 3-a. Evolution of $\|u_1(t) - \bar{u_1}\|_{L^1}$ for large simulation time $\Delta t = 0.05$, $\Delta\lambda = \pi/96$ and $\Delta\phi = \pi/96$

$$
\begin{aligned}
u_3(0,x) &= \begin{cases} \theta e^{x_3} + e^{\theta}, & -\sqrt{3} \le \theta \le 0, \\ -1 + \theta\log(\theta), & \text{otherwise.} \end{cases} \\
u_4(0,x) &= \begin{cases} x_2\sinh(x_1) + \frac{1}{x_1^2+4}, & -1 \le x_1 \le 0, \\ -\cosh(x_1)/4, & \text{otherwise.} \end{cases}
\end{aligned}
\tag{6.3}
$$

Figures 26 and 25 present the evolution of the parameter $\|\partial_t u\|_{\mathcal{M}}(t)$ for the

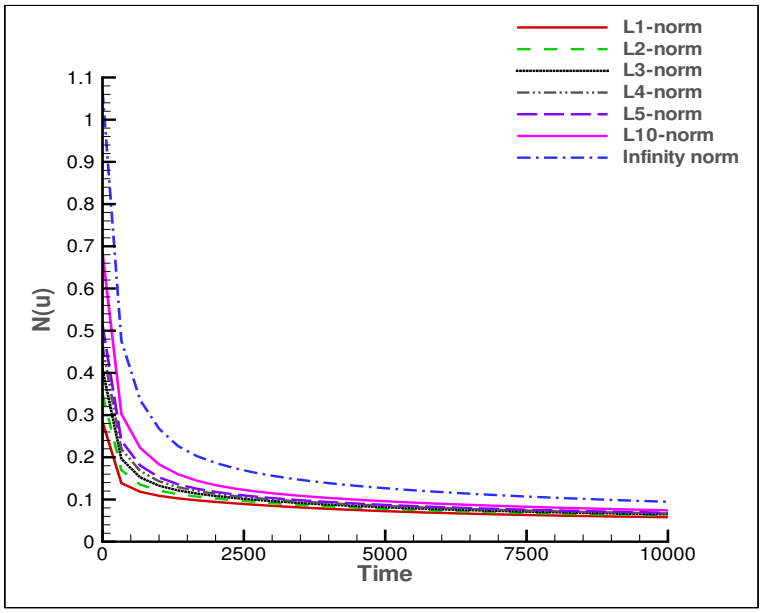

Figure 24. Stability property for Test 3-a at time $t = 100$ with $\Delta t = 0.01$, $\Delta\lambda = \pi/96$ and $\Delta\phi = \pi/96$.

first and second order schemes, respectively. As can be seen in these figures, this parameter decreases over time, which shows that the time-variation diminishing property 1.4 is valid for all the functions arbitrarily chosen.

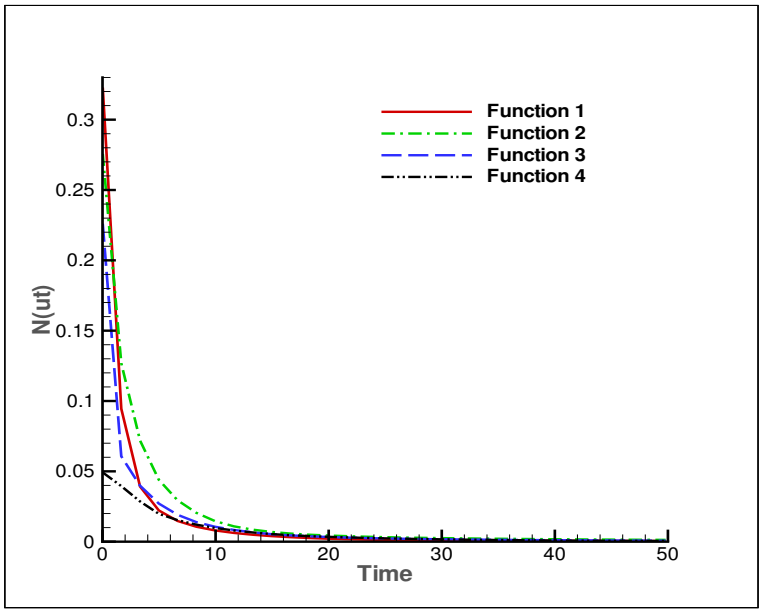

Figure 25. Property (2.8) for the first order scheme until time $t = 50$ with $\Delta t = 0.01$, $\Delta\lambda = \pi/96$ and $\Delta\phi = \pi/96$.

The contraction property 1.5 is now checked for the first order scheme using

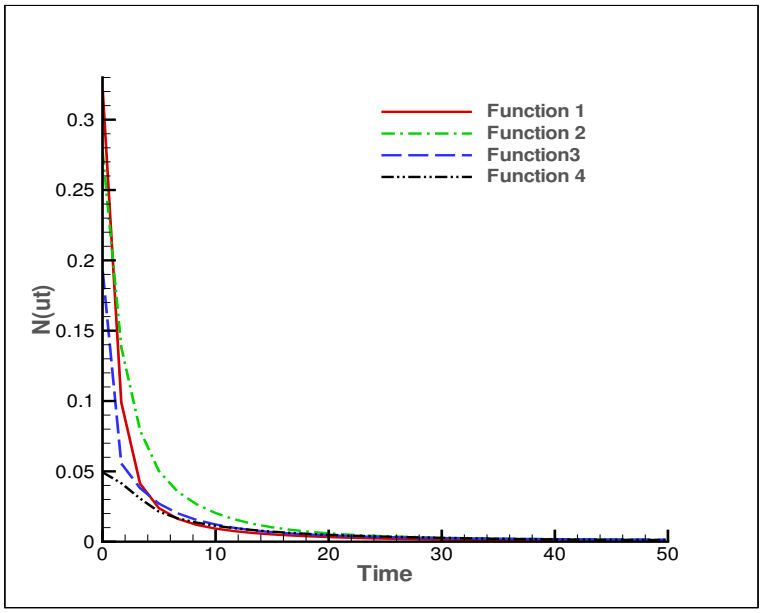

Figure 26. Entropy stability property 1.3 for the second order scheme until time $t = 50$ with $\Delta t = 0.01$, $\Delta\lambda = \pi/96$ and $\Delta\phi = \pi/96$.

the following pairs of functions.

$$
\begin{aligned}
v_1(0,x) &= \begin{cases} x_2\theta + \cosh(\theta), & -\sqrt{3} \le \theta \le 0, \\ x_2\theta - \cosh(\theta), & \text{otherwise.} \end{cases} \\
w_1(0,x) &= \begin{cases} x_2, & -\sqrt{3} \le \theta \le 0, \\ -x_2, & \text{otherwise.} \end{cases}
\end{aligned} \tag{6.4}
$$

$$
\begin{aligned}
v_2(0,x) &= \begin{cases} 1, & 0 \le \lambda \le \pi, \\ \cos(\lambda), & \text{otherwise.} \end{cases} \\
w_2(0,x) &= \begin{cases} \arcsin(x_2), & 0 \le \lambda \le \pi, \\ \cos(\lambda)\arcsin(x_2), & \text{otherwise.} \end{cases}
\end{aligned} \tag{6.5}
$$

$$
\begin{aligned}
v_3(0,x) &= \begin{cases} e^{\theta}x_1x_2x_3, & -\sqrt{3} \le \theta \le 0, \\ -x_1x_2x_3, & \text{otherwise.} \end{cases} \\
w_3(0,x) &= \begin{cases} x_2x_3, & -\sqrt{3} \le \theta \le 0, \\ -x_2x_3 + e^{-1/\theta}, & \text{otherwise.} \end{cases}
\end{aligned} \tag{6.6}
$$

$$
\begin{aligned}
v_4(0,x) &= \begin{cases} \frac{\theta^2+1}{2-\theta}, & -\sqrt{3} \le \theta \le 0, \\ x_2\theta - 1/2, & \text{otherwise.} \end{cases} \\
w_4(0,x) &= \begin{cases} \frac{e^{\theta}}{\theta-1}, & -\sqrt{3} \le \theta \le 0, \\ \frac{\cosh(\theta)}{1+\theta} + x_3\theta, & \text{otherwise.} \end{cases}
\end{aligned} \tag{6.7}
$$

$$
\begin{aligned}
v_5(0,x) &= \begin{cases} \theta, & \theta \leq 1, \\ \frac{x_1 \log(\theta)}{\theta} - \theta, & \text{otherwise.} \end{cases} \\
w_5(0,x) &= \begin{cases} \theta - 2\theta^3, & \theta \leq 1, \\ \frac{1}{\theta} + x_2 \log(\theta), & \text{otherwise.} \end{cases}
\end{aligned}
\tag{6.8}
$$

As shown in Figure 27 the ratios $E(v,w)$ are decreasing for all pairs of the functions which confirms that the contraction property 1.5 is valid for all those pairs of functions.

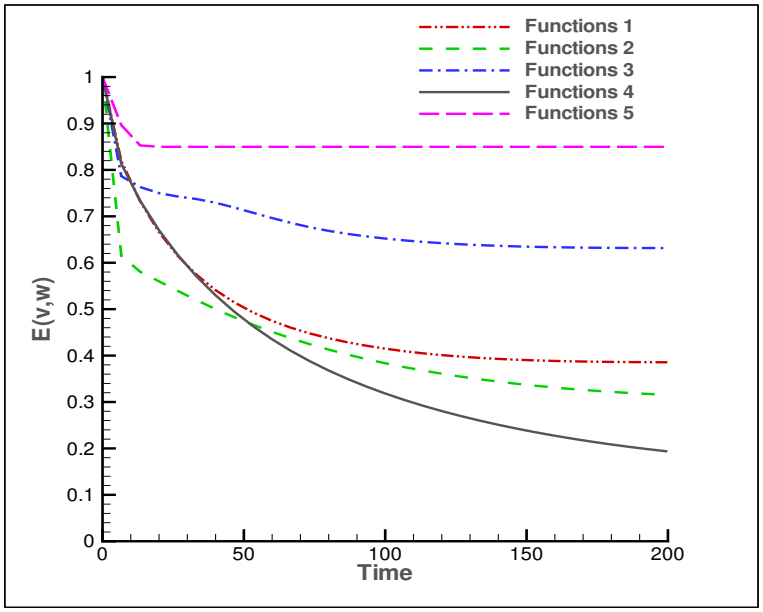

Figure 27. Contraction property 1.5 for the first order scheme with $\Delta t = 0.01$, $\Delta\lambda = \pi/96$ and $\Delta\phi = \pi/96$.

7 Fourth test case with fully coupled flux vector fields

In this section we consider a generic flux defined on the basis of the parameterized scalar potential composed of two different terms in order to ensure the generic behavior.

$$
\begin{aligned}
h(x,u) &= H_1(x) f_1(u) + H_2(x) f_2(u), \\
H_1(x) &= x_1, \qquad H_2(x) = x_2, \\
f_1(u) &= s u^2/2, \quad f_2(u) = s^{'} u^3/3, \quad s + s^{'} = 1.
\end{aligned}
\tag{7.1}
$$

The setting of the value of the parameter s allows us to observe several characters of solutions and to study the impact of each part of the scalar potential on the evolution of these solutions and their late-time asymptotic behaviors.

We present a synthesis of the tests performed and, first we consider the initial condition u_2 given in test 2-b defined by the equation (5.4). The test 2-b given in Section 2 corresponds to the particular case in which $s = 1$. For this case, as mentioned before, the solution evolves to two constant values in two independent domains. If the parameter $s = 0.95$ is used with the same initial condition u_2, both terms of the potential flux have an impact on the solution, continuously over time, which converges to one constant value in the entire sphere.

Figure 28 shows the convergence curves relating the evolution of the parameter $\|u_2(t) - \bar{u_2}\|_{L^1}$ for different values of the parameters s. For all values of the parameter s presented in figure 28, the solution converges to one constant value in the entire sphere. As can be seen in this figure, the behaviors of the solutions is complex depending on the choice of the parameter s. The evolution of the solutions is highly influenced by the magnitude of the different components of the potential function and the nature of the initial condition.

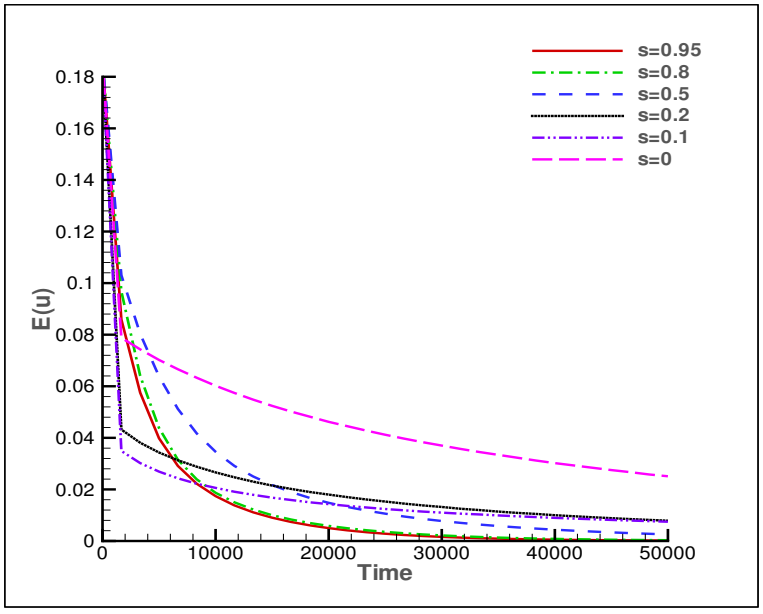

Figure 28. Convergence for Test 4: Evolution of the parameter $E(u) = \|u_2(t) - \bar{u_2}\|$ for generic flux with different values of the parameter s with $\Delta t = 0.05$, $\Delta\lambda = \pi/96$ and $\Delta\phi = \pi/96$

The entropy stability property 1.3 is now checked for the generic flux corresponding to $s = 0.5$. Figure 29 shows the evolution of the parameter $\|u_2(t)\|_{L^p_\omega(M)}$ for $p = 1, 2, 3, 4, 5, 10$ and $p = \infty$. According to this figure, we conclude that the solution u_2 satisfies the entropy stability property for all L^p norms considered.

For the generic flux with $s = 0.5$, the time-variation diminishing property 1.4 is checked for the second order scheme using the five initial conditions

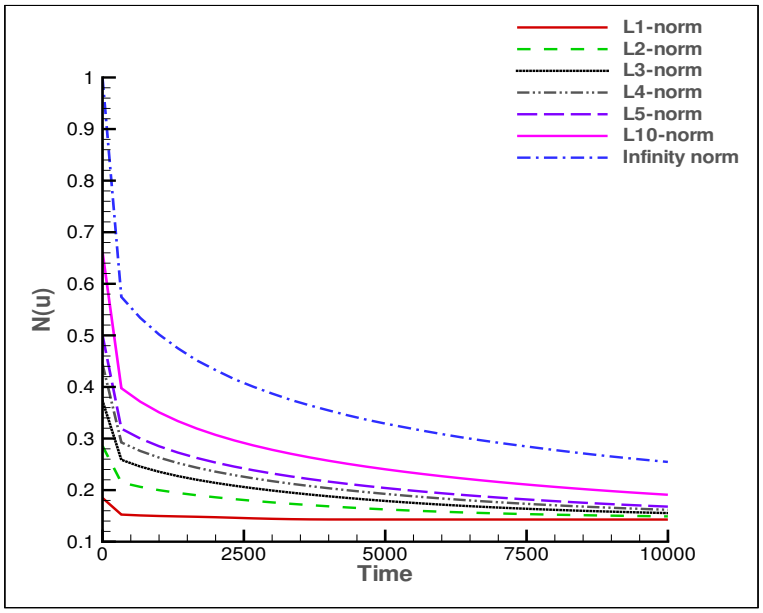

Figure 29. Entropy stability property 1.3 for the generic flux with $\Delta t = 0.01$, $\Delta\lambda = \pi/96$ and $\Delta\phi = \pi/96$.

u_0, u_1, u_2, u_3 and u_4, defined before in the second test. Figure 30 presents the evolution of the parameter $\|\partial_t u\|_{\mathcal{M}}(t)$ and confirms that this parameter decreases with time, which shows that the time-variation diminishing property holds for those functions.

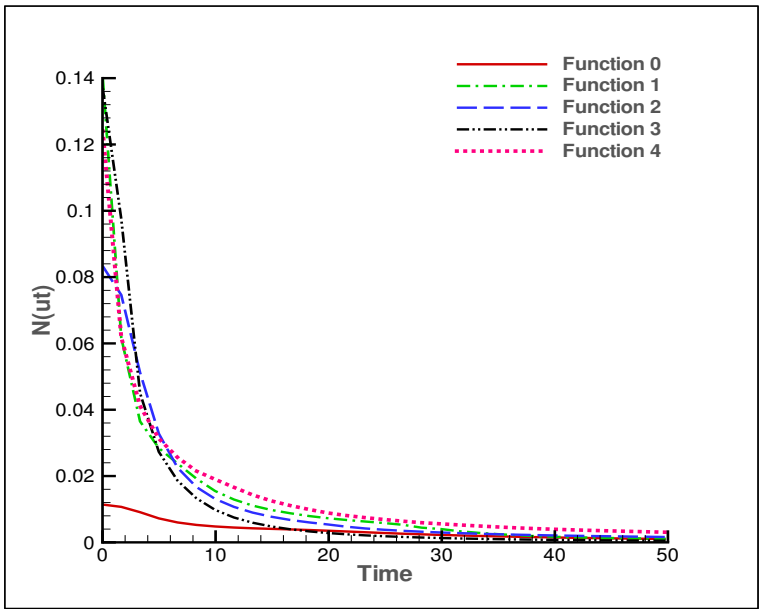

Figure 30. Time-variation diminishing property 1.4 for the generic flux using the second order scheme with $\Delta t = 0.01$, $\Delta\lambda = \pi/96$ and $\Delta\phi = \pi/96$.

The five pairs of functions defined in test 2 are used to verify the contraction property 1.5 for the first order scheme using the generic flux with $s = 0.5$.

Figure 31 shows the evolution of the ratio parameter $E(v, w)$ for the five pairs of functions. This parameter is decreasing for all the pairs of initial conditions which confirms that the contraction property holds for these pairs of functions.

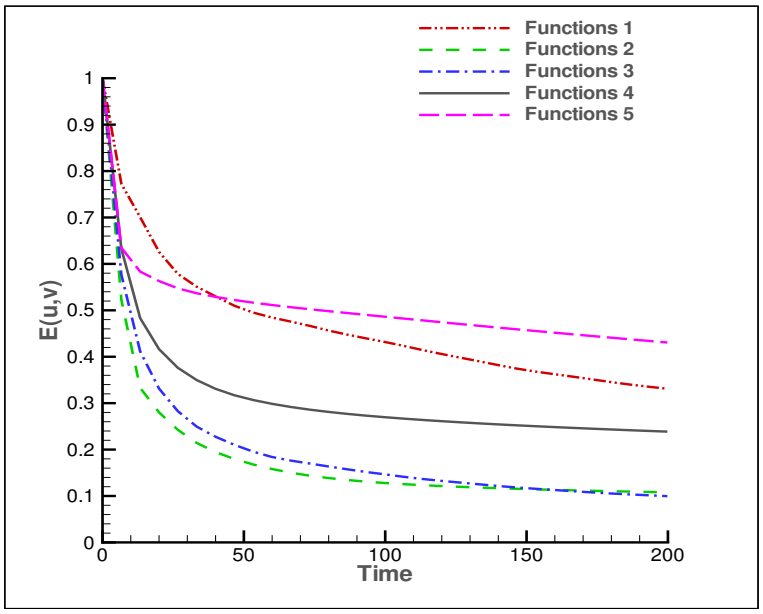

Figure 31. Contraction property 1.5 for the first order scheme with $\Delta t = 0.01$, $\Delta\lambda = \pi/96$ and $\Delta\phi = \pi/96$.

8 Fifth test case: revisiting the asymptotic convergence property

The aim of this section is to complete the analysis of the behavior of the solutions of the equation (2.10) for nonlinear foliated flux. We present some examples in order to cover all cases of asymptotic convergence of the solutions when the nonlinear foliated fluxes are considered.

In the cases already seen in test 2 and test 3 for the asymptotic convergence of the solutions for nonlinear foliated flux, we observe numerically that the solution converges to constant values on independent domains on the sphere. This is a particular case of what is generally observed if the numerical scheme is more accurate and capable of simulating the solutions for large simulation time. Then, in order to cover the other behaviors we give more attention to the accuracy of the used scheme. To achieve this goal we consider the same second geometry-compatible finite volume scheme by considering a computational cell in which the sides are a part of the level sets and their equipotential curves.

We consider the nonlinear foliated flux defined on basis of the scalar potential function $h(x, u) = -x_3u^2/2$. For this flux the level sets are the curves defined by $\phi = \phi_c$, where ϕ_c is a real constant in $[-\pi/2, \pi/2]$. The obtained level sets

coincide with the grid used which ensures a very good accuracy of the scheme. In the following, we present the results for two cases with different forms of the functions considered as initial conditions. The first initial condition $u_1(0,x)$ is defined as follows:

$$u_1(0,x) = \begin{cases} x_1 + \sin \lambda x_2, & 0 \leq \lambda \leq \pi, \\ -x_1 + \sin \lambda x_2, & \text{otherwise.} \end{cases} \tag{8.1}$$

and the second initial condition $u_2(0,x)$ is defined by:

$$u_2(0,x) = \begin{cases} x_2 + \sinh(x_1)\cos(\lambda), & 0 \leq \lambda \leq \pi/2, \\ -x_2, & \pi/2 < \lambda < \pi, \\ x_2 + \cosh(x_3)\sin(\lambda), & \text{otherwise.} \end{cases} \tag{8.2}$$

Figures 32 and 33 respectively show the two-dimensional view of the first initial condition u_1 and the corresponding solution for long simulation time. The two-dimensional view of the second initial condition u_2 and the corresponding solution for long simulation time are shown in figure 34 and 35, respectively.

According to the numerical results shown in those figures for the two cases studied, the solution remains unchanged after a certain time. The solution converges to a nontrivial stationary solution which is constant on each level set.

From the numerical tests one can conclude that, given any nonlinear foliated flux and any arbitrary function taken as initial condition, the solution of the equation (2.10) converges to a steady sate solution which is in general nontrivial and constant on the level sets. Each constant convergence value is the average value on the corresponding level set of the function taken as initial condition.

We conclude this section by noting our important result which has a very significant positive effect for the performance of the numerical schemes in the case of nonlinear foliated fluxes. For this type of flux we recommend the use of a computational cell which is compatible with the level sets of the flux. More precisely we can use a subset of the level sets and their orthogonal equipotentials of the nonlinear foliated flux as the constructing lines of computational cells.

Using a choice of this kind, a very good conservation of nontrivial stationary solutions is guaranteed which enormously improves the accuracy of the schemes when more general solutions are considered.

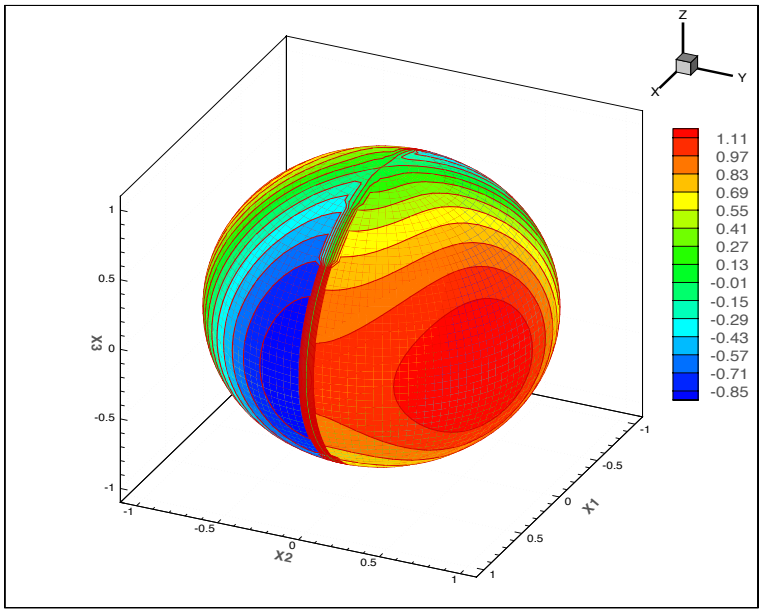

Figure 32. Initial condition u_1 with $\Delta\lambda = \pi/96$ and $\Delta\phi = \pi/96$.

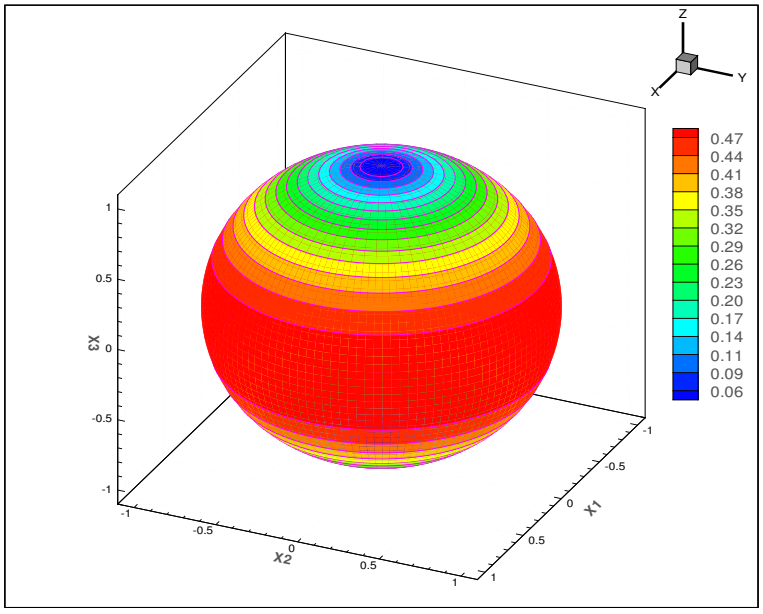

Figure 33. Solution u_1 at time $t = 50000$ with $dt = 0.05$, $\Delta\lambda = \pi/96$ and $\Delta\phi = \pi/96$.

9 Concluding remarks

In this paper, we have analyzed a class of nonlinear hyperbolic conservation laws posed on the sphere. The first- and second-order versions of the proposed geometry-compatible finite volume scheme (based on generalized Riemann solvers and on an operator splitting approach) were investigated, and we numerically established several important properties enjoyed by discontinuous solutions defined on a curved geometry, including the contraction, time-variation monotonicity, and the entropy monotonicity properties.

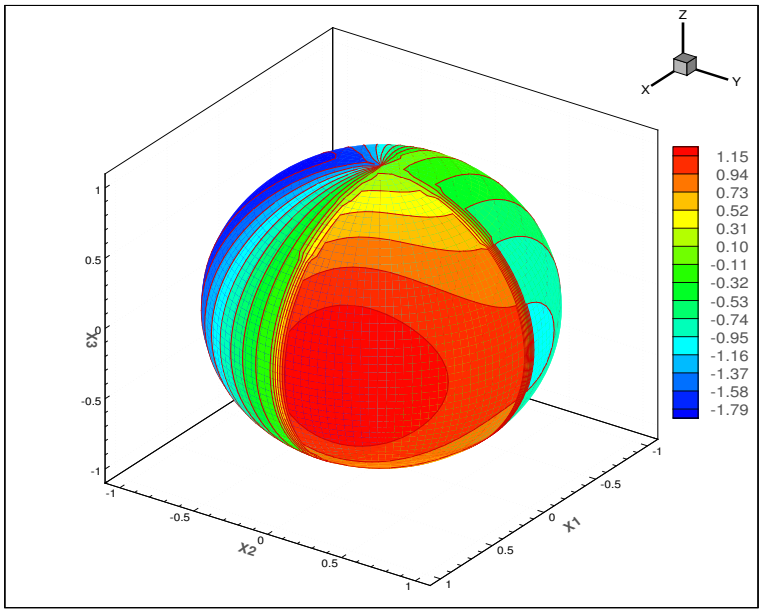

Figure 34. Initial condition u_2 with $\Delta\lambda = \pi/96$ and $\Delta\phi = \pi/96$.

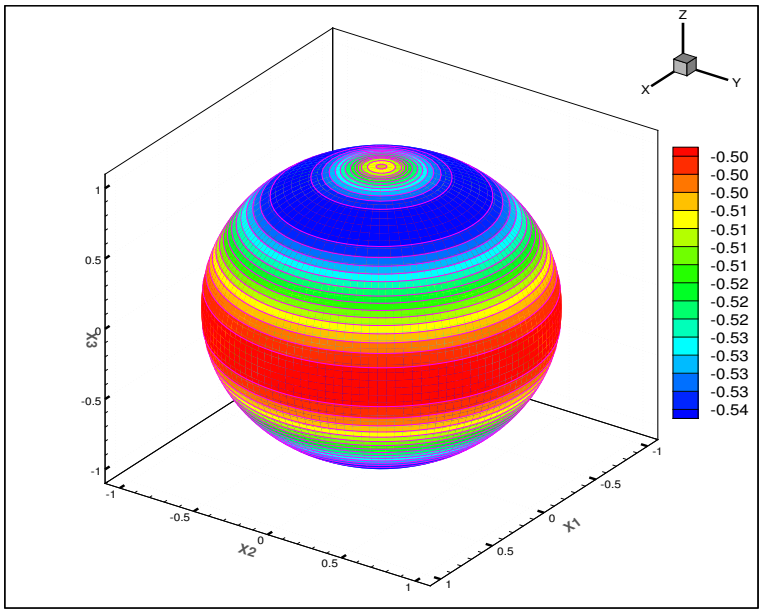

Figure 35. Solution u_2 at time $t = 50000$ with $dt = 0.05$, $\Delta\lambda = \pi/96$ and $\Delta\phi = \pi/96$.

Furthermore, we carefully investigated the late-time asymptotic behavior of solutions, by distinguishing various types of flux potential. The following main conclusions were established for the class of nonlinear hyperbolic conservation laws and the finite volume schemes under consideration:

- The entropy stability property is valid in all L^p norms with $p \in [1, +\infty)$, and the time-variation diminishing property is satisfied by the first- and second-order schemes.
- The contraction property is satisfied by the first-order scheme but, as might

be have been expected, this property is not valid for the second-order method.

- Two classes of flux were distinguished according to the structure of the flux potential. We introduced the notions of foliated flux and generic flux. The late-time asymptotic behavior of solutions was found to strongly depend on the flux (foliated or generic) as well as its (linearity or) nonlinearity.
- Specifically, when the flux is foliated and linear, the solutions are transported in time within the level sets of the potential.
- When the flux is foliated and is genuinely nonlinear, the solutions converge to their (constant) average within each level set.
- For generic flux, the solutions evolve with large variations which depend on the geometry. and converge to constant values within certain "independent" domains defined on the sphere. The number of constant values depends on curves that "split" the sphere into possibly several independent domains.
- Last but not least, we have an important conclusion about the performance of the numerical schemes for the foliated flux, for which the level sets play an essential role in understanding the evolution of solutions; this is especially true for genuinely nonlinear foliated flux. For such flux, we strongly recommend the use of a suitable computational mesh not only in terms of space constraints and the desired accuracy which are commonly used for the choice of the mesh, but also according to the physical phenomenon studied. The latter is reflected by the flux. More precisely, we recommend the use of a subset of the level sets of the nonlinear foliated flux as the construction lines of the computational grids. When this adjustment is respected, the steady sate solutions for the nonlinear foliated flux can be captured with more accuracy and better results can be obtained for general solutions.

References

[1] P. Amorim, M. Ben-Artzi and P.G. LeFloch, Hyperbolic conservation laws on manifolds: Total variation estimates and finite volume method, Meth. Appl. Analysis 12 (2005), 291–324.

[2] P. Amorim, P.G. LeFloch, and B. Okutmustur, Finite volume schemes on Lorentzian manifolds, Comm. Math. Sc. 6 (2008), 1059–1086.

[3] M. Ben-Artzi and J. Falcovitz, *Generalized Riemann problems in computational fluid dynamics*, Cambridge University Press, London, 2003.

[4] M. Ben-Artzi, J. Falcovitz, and P.G. LeFloch, Hyperbolic conservation laws on the sphere. A geometry-compatible finite volume scheme, J. Comput. Phys. 228 (2009), 5650–5668.

[5] M. Ben-Artzi and P.G. LeFloch, The well posedness theory for geometry compatible hyperbolic conservation laws on manifolds, Ann. Inst. H. Poincaré Anal. Non Linéaire 24 (2007), 989–1008.

[6] M.J. Berger, D.A. Calhoun, C. Helzel, and R.J. LeVeque, Logically rectangular finite volume methods with adaptive refinement on the sphere, Philos. Trans. R. Soc. Lond. Ser. A 367 (2009), 4483–4496.

[7] A. Bourgeade, P.G. LeFloch, and P.-A. Raviart, An asymptotic expansion for the solution of the generalized Riemann problem. Part II. Application to the gas dynamics equations, Ann. Inst. H. Poincaré, Nonlin. Anal. 6 (1989), 437-480.

[8] G.J. Haltiner, *Numerical weather prediction*, John Wiley Press, 1971.

[9] S.N. Kruzkov, First-order quasilinear eequations in several independent variables, Math. USSR Sb. 10 (1970), 217–242.

[10] P.G. LeFloch, Hyperbolic conservation laws on spacetimes, in "Nonlinear conservation laws and applications", IMA Vol. Math. Appl. 153, Springer, New York, 2011, pp. 379–391.

[11] P.G. LeFloch and H. Makhlof, A geometry-preserving finite volume method for compressible fluids on Schwarzschild spacetime, Commun. Comput. Phys. (to appear). See also ArXiv:1212.6622.

[12] P.G. LeFloch, H. Makhlof, and B. Okutmustur, Relativistic Burgers equations on curved spacetimes. Derivation and finite volume approximation, SIAM J. Numer. Anal. 50 (2012), 2136–2158.

[13] P.G. LeFloch and B. Okutmustur, Hyperbolic conservation laws on spacetimes. A finite volume scheme based on differential forms, Far East J. Math. Sci. 31 (2008), 49–83.

[14] P.G. LeFloch and P.-A. Raviart, An asymptotic expansion for the solution of the generalized Riemann problem. Part I. General theory, Ann. Inst. H. Poincaré, Nonlinear Analysis 5 (1988), 179–207.

[15] R.J. LeVeque, Balancing source terms and flux gradients in high-resolution Godunov methods: The quasi-steady wave-propagation algorithm, J. Comput. Phys (1998), 346–365.

[16] R.J. LeVeque, *Finite volume methods for hyperbolic problems*, Cambridge University Press, Cambridge, 2002.

[17] C. Ronchi, R. Acono, and P.S. Paolucci, The cubed sphere: a new method for the solution of partial differential equations in spherical geometry, J. Comput. Phys. 124 (1996), 93–114.

[18] A. Rossmanith, D.S. Bale, and R.J. LeVeque, A wave propagation algorithm for hyperbolic systems on curved manifolds, J. Comput. Phys. 199 (2004), 631–662.

[19] A. Rossmanith, A wave propagation method for hyperbolic systems on the sphere, J. Comput. Phys. 213 (2006), 629–658.